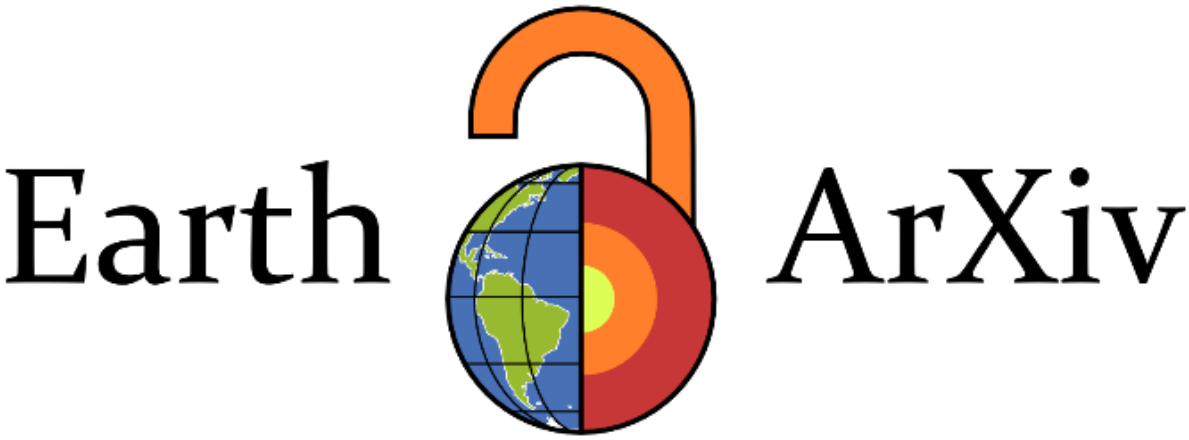

Highlights

Temperature Insensitive Viscous Deformation Limits Megathrust Seismogenesis

[a,b]Liam Moser, [b]Matěj Peč, [b]Camilla Cattania

- The depth limits of subduction seismogenic zones are ∼50 km across a >250°C range
- The depth limit is not controlled by the classic 350°C or overriding plate Moho model
- A temperature insensitive frictional-viscous transition fits observations to ∼6 km
- Talc low-T plasticity and a weak ($\mu \lesssim 0.1$) megathrust fit the observed depth limits

Temperature Insensitive Viscous Deformation Limits Megathrust Seismogenesis

[a,b]Liam Moser, [b]Matěj Peč, [b]Camilla Cattania

[a]*The MIT-WHOI Joint Program in Oceanography/Applied Ocean Science and Engineering, Cambridge and Woods Hole, MA, USA*
[b]*Department of Earth, Atmospheric and Planetary Sciences, Massachusetts Institute of Technology, Cambridge, MA, USA*

Abstract

Three models have been proposed to explain the downdip limit of the subduction seismogenic zone. The first is a temperature-controlled transition in rate-and-state frictional properties between 350–510°C, which inhibits earthquake nucleation. The second places the limit at the frictional and viscous failure envelope intersection. The third combines thermal and lithological controls, where 'warm' subduction zones are controlled by a 350°C frictional transition and 'cold' subduction zones are limited by the overriding plate Moho. To evaluate these hypotheses, we integrate thermal models with seismicity catalogs from 17 subduction zones. Observed depth limits remain remarkably consistent (∼50 km) across a temperature range exceeding 250°C, indicating that the temperature-controlled rate-and-state friction model cannot fully explain observed depths. While warm subduction zones can be reasonably explained as a rate-and-state stability transition, the overriding plate Moho in cold subduction zones is too shallow, challenging the combined thermal-lithological model. To test the frictional-viscous model, we analyze power law creep and low-temperature plasticity for quartz, feldspar, olivine, antigorite, and talc. We find that power law creep in any tested mineral is overly temperature sensitive. In contrast, wet olivine, antigorite, and talc low-temperature plasticity fits observed depth limits to a ∼6 km misfit. However, only talc is consistent with the weak megathrust paradigm of effective friction coefficients <0.1 and shear strengths of tens of MPa. We conclude that a frictional-viscous transition with a weak and temperature-insensitive viscous mechanism, such as talc low-temperature plasticity, is most consistent with the downdip seismicity limit and constraints on megathrust strength.

Preprint submitted to Earth and Planetary Science Letters (Accepted) November 7, 2025

Keywords: Earthquakes, Subduction Zones, Friction, Rheology, Fault Mechanics

1. Introduction

Subduction zones host Earth's largest earthquakes (Lay et al., 2005), and the along-dip extent of seismic ruptures constrains the intensity of damaging ground shaking onshore. We define the subduction seismogenic zone as the depth range over which interplate thrust earthquakes are nucleated, and we investigate the mechanisms that control its downdip limit. Since large megathrust earthquakes often nucleate near this boundary, understanding the dominant deformation mechanisms at the downdip limit offers critical insight into the conditions that initiate such events.

Three main mechanisms have been proposed to explain the downdip extent of the subduction seismogenic zone (Fig. 1). First, in the *rate-and-state model*, seismogenesis is limited by a thermally controlled transition in fault rock frictional properties - from velocity-weakening to velocity-strengthening - which inhibits earthquake nucleation beyond a critical temperature (e.g., Liu and Rice, 2009; Wang and Tréhu, 2016; Erickson et al., 2020). Lab experiments on fault gouge material place the transition at 350–510°C. This view is supported by the depth distribution of seismicity and slip behavior on crustal faults (Scholz, 1998; Tse and Rice, 1986), and has been proposed as a control for subduction zone earthquakes as well (Scholz, 1998). Second, the *frictional-viscous model* attributes the depth limit to a competition between frictional failure on localized faults and distributed viscous flow. The maximum earthquake depth is then determined by the intersection of frictional and viscous failure envelopes, confining earthquakes to the frictional regime, where the intersection is primarily controlled by temperature, lithology, and strain rate (e.g., Sibson, 1982; Gao and Wang, 2017; Condit et al., 2022). Third, the *Moho control model* incorporates both thermal and lithological controls: in warm subduction zones, as in the first model, the depth limit is governed by a rate-and-state friction transition, while in cold subduction zones it is constrained by the depth of the overriding plate Moho and associated lithological changes (Hyndman et al., 1997; Oleskevich et al., 1999). It is proposed that hydration of the ultramafic wedge by fluids from the downgoing slab produces velocity-strengthening serpentine minerals that inhibit seismic slip (Hyndman et al., 1997; Peacock and Hyndman, 1999; Moore et al., 1997).

In this work, we re-evaluate the viability of the rate-and-state and Moho control models using recent global subduction thermal models and seismic observations (van Keken et al., 2018; Heuret et al., 2011; Hayes et al., 2018). We show that neither model adequately explains the observed depth limits and that our work is consistent with the growing consensus that the overriding plate Moho does not control the depth limit of seismogenic rupture (Peacock and Bostock, 2024; Wang et al., 2025). We then explore whether the downdip limit of observed seismicity is controlled by a frictional-viscous transition (FVT) model. For the transition to viscous deformation, we consider power law creep, which has been extensively studied both theoretically and experimentally, and is commonly used as a candidate mechanism to halt frictional failure (e.g., Condit et al., 2022; Gao and Wang, 2017). We also include low-temperature plasticity (LTP), which has emerged as a likely deformation mechanism under the relatively low-temperature, high-stress conditions typical of subduction fault zones (Hirauchi et al., 2010; Aharonov and Scholz, 2019; Wang, 2024; Wang et al., 2025; Wang and He, 2025).

A wide array of materials has been proposed to govern the downdip limit, including basalt (Liu and Rice, 2009), schist (Condit et al., 2022), serpentinites (Wang et al., 2025; Hirauchi et al., 2010), quartzo-feldspathic rocks (Oleskevich et al., 1999), mudstones (Fisher and Hirth, 2024), and specific minerals such as talc (Horn and Skemer, 2023; Boneh et al., 2023). Here we consider all minerals for which we have both well-constrained power-law and LTP experimental data. Thus, we analyze quartz, feldspar, and olivine and identify the temperature and stress sensitivity that any mechanism must exhibit to match observed depth limits. In addition, we extend LTP to antigorite and talc, both byproducts of olivine serpentinization. Our analysis demonstrates that any candidate mechanism must be extremely temperature insensitive, predict a transition to viscous creep near 50 km depth, and allow for an effective friction coefficient $\mu' < 0.1$. Among published rheologies, a LTP flow law for talc recently proposed by Shabtian and Hirth (2025), combined with $\mu \lesssim 0.05$, produces the best fit to the global earthquake depths, suggesting that talc may play an important role in inhibiting seismogenesis along the megathrust.

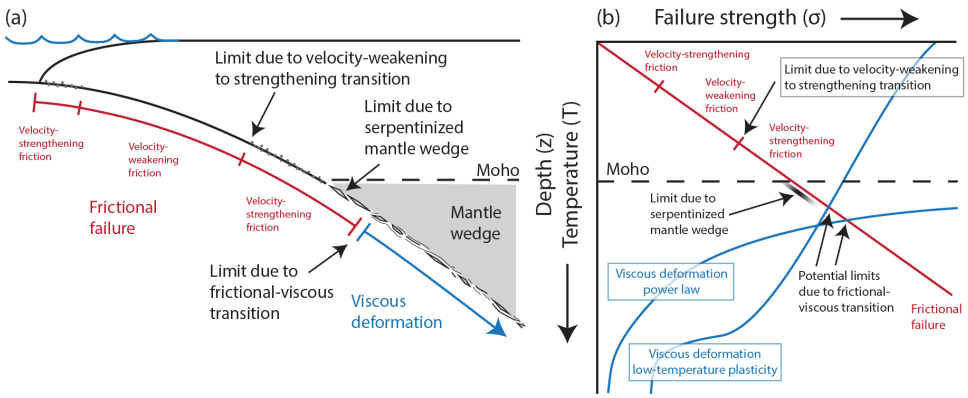

Figure 1: Schematic of different processes hypothesized to control the downdip limit of the megathrust seismogenic zone presented (a) along a subduction zone and (b) as a yield strength diagram.

2. Data Overview

2.1. Observing the Megathrust Seismogenic Zone

The subduction zone seismogenic depth limit inherently depends on how it is defined (Wang and Tréhu, 2016). Definitions based on geodetically inferred plate locking, great earthquake rupture extent, and distribution of small to medium earthquakes need not share the same depth limit. Thus, comparison across definitions must be done with caution as the underlying physics of the observation may not be the same. To avoid conflating definitions, we focus on earthquake nucleation and the depth of extent of small to medium earthquake hypocenters from global teleseismic catalogs.

We take the observed downdip limits of the subduction seismogenic zone from two independent sources: Heuret et al. (2011) and Hayes et al. (2018) (Slab2). Heuret et al. (2011) uses thrust-event detections of 5.5 $\leq$M$<$ 7 from the Harvard Centroid Moment Tensor catalog (Dziewonski et al., 1981) with hypocenter locations dictated by the EHB bulletin (Engdahl et al., 1998). The 95^{th} percentile of this earthquake depth distribution sets the depth limit, and zones with N$<$10 earthquakes are defined as poorly constrained. Slab2 uses thrust events from the Advanced National Seismic System Combined Catalog (ComCat) and fits them with a double-normal distribution, with the 90^{th} percentile setting the depth limit and a threshold of N$<$50 for poorly constrained zones. Heuret et al. (2011) breaks the global subduction system into 62 segments, of which we match 17 with both Slab2 and the thermal

models (Table S1). In addition, we use the constraint thresholds to define a well-constrained subset of subduction zones for testing. The Supplementary Material further discusses Heuret et al. (2011) and Slab2 and makes comparisons to regional studies.

2.2. Subduction Zone Thermal Models

We utilize two independent sets of subduction zone finite element thermal models, vK11m and WW09m, from van Keken et al. (2018) to map the temperature along the downgoing slab. Both models solve the Stokes and heat equations, but make different assumptions on prescribed slab velocity and heat transfer, with WW09m assuming steady-state temperature.

The thermal state boundary condition is a one-dimensional slab temperature profile on the seaward model edge. This profile is set by plate cooling at the given plate age and, in the case of WW09m, includes the effect of sedimentation. Temperatures at different depths below the slab top are reported in van Keken et al. (2018) and we use the shallowest case of 0.5 km. We use models with shear heating from an effective friction coefficient of $\mu'_{sh} = 0.03$ and $\mu'_{sh} = 0.12$, representative values that match observed heat flow (van Keken et al., 2018; Gao and Wang, 2014). Petrological estimates of the geotherm are 100-300°C warmer than thermal models, regardless of slab speed or age (Penniston-Dorland et al., 2015). However, the accuracy of petrological results versus thermal modeling is heavily debated and we focus on thermal models as they provide the depth resolution needed for our analysis (van Keken et al., 2018).

Subduction zones, when plotted as the independent variable, are sorted from cold to warm by thermal parameter from van Keken et al. (2018) (e.g., Fig. 2), defined as

$$\phi = V_p A_p \sin \Delta \tag{1}$$

where V_p is incoming plate velocity, A_p incoming plate age, and Δ slab dip (Molnar et al., 1979; Kirby et al., 1991).

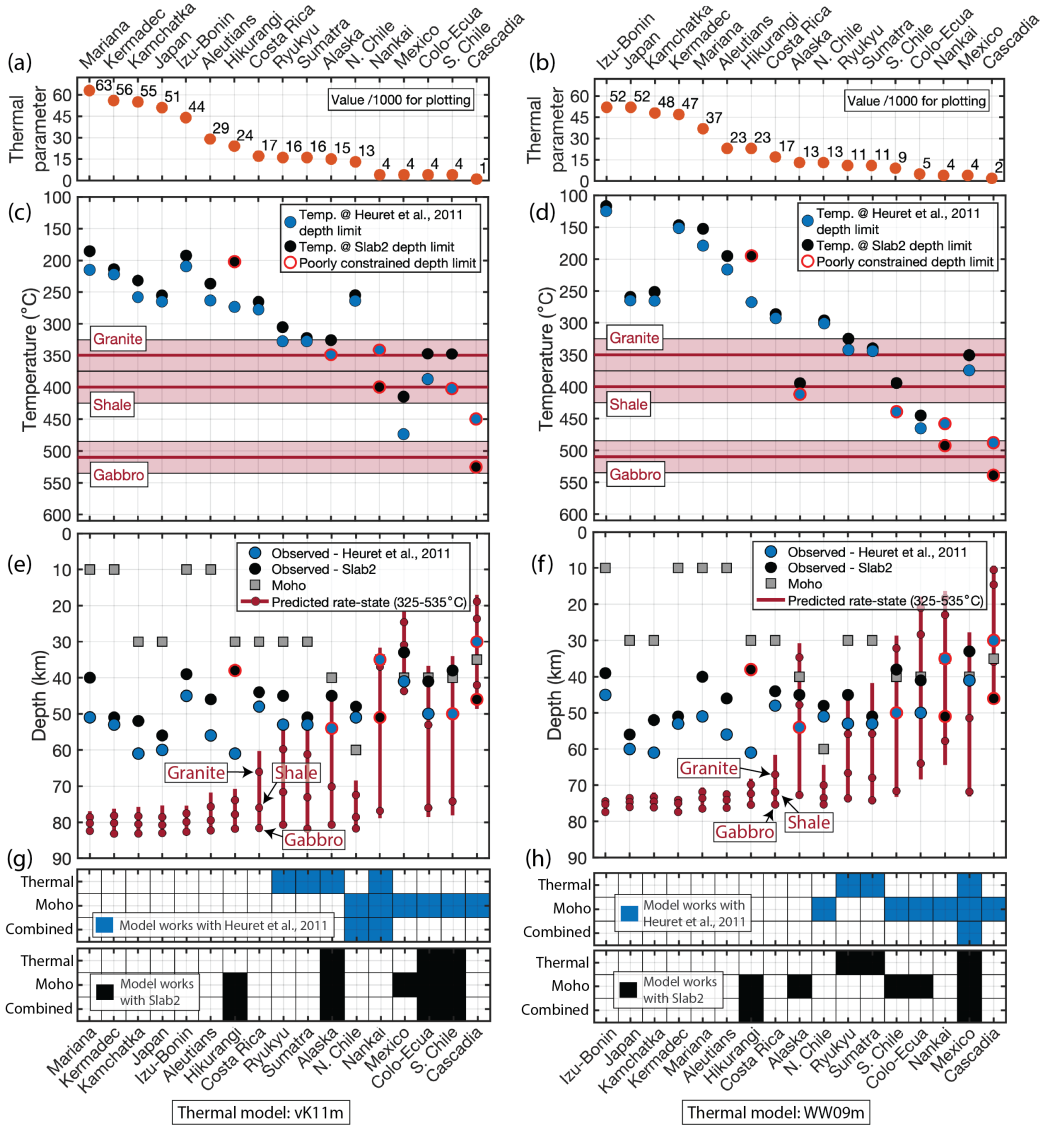

Figure 2: Analysis of both rate-and-state and Moho control model efficacy across 17 subduction zones. The left column uses the vK11m thermal model and the right WW09m. (a, b) Subduction zones sorted by thermal parameter. (b, c) Temperature at the observed depth limits for Heuret et al. (2011) (blue circles) and Slab2 (black circles) compared to laboratory predictions of the transition from velocity-weakening to strengthening friction for different gouge materials (red lines). Red shaded regions are ±25°C uncertainty (Oleskevich et al., 1999). Red circle edges are depth limits defined as poorly constrained by source (earthquakes N, <50 for Slab2, <10 for Heuret et al. (2011)).

Figure 2: (e, f) Comparison of observed depth limits, overriding plate Moho depth, and the rate-and-state predicted depth limit range. Blue and black circles are Heuret et al. (2011) and Slab2 depth limits, respectively. Gray squares mark Moho depth. Red lines mark the rate-and-state prediction for the granite-gabbro velocity-weakening to strengthening temperature range (325-535°C) shown in c, d. (g, h) Summary of how observed depth limits are fit by both mechanisms in the Moho control model."Thermal" denotes that the temperature at the observed depth limit is 350±25°C and is thus is explained by the granite rate-and-state data."Moho" denotes a depth limit within 10 km from the overriding plate Moho depth. Combined denotes the full Moho control model works, which requires the shallower criteria to be successful.

3. Evaluating the Rate-and-State and Moho Control Models

3.1. Model Background

The ability to nucleate earthquakes in rate-and-state friction is controlled by the parameter $a - b$. Steady-state friction is given by

$$\mu(V) = \mu_0 + (a - b) \ln \left(\frac{V}{V_0} \right), \tag{2}$$

where V is slip velocity, V_0 the reference velocity, μ_0 the reference coefficient of friction at V_0, and a and b are rate-and-state parameters (Ruina, 1983; Dieterich, 1979). When $a - b < 0$ a fault is velocity-weakening as steady-state friction decreases with increasing V, allowing earthquake nucleation.

Rate-and-state friction experiments show temperature-dependent parameters (Blanpied et al., 1998; He et al., 2007; den Hartog and Spiers, 2013). These experiments define a range of temperatures where rate-and-state parameter $a - b < 0$ (Fig. S9b). The velocity-weakening range is 90-360°C for granite gouge (Blanpied et al., 1998), approximately 200-510°C for gabbro gouge (He et al., 2007), and 250-400°C for an illite-rich shale gouge (den Hartog and Spiers, 2013). Aseismic slip occurs both up and downdip of the subduction seismogenic zone and is defined as a velocity-strengthening frictional regime ($a-b > 0$), thus the temperature ranges bound the velocity-weakening subduction seismogenic zone (Scholz, 1998). Combining the lab-constrained temperature with an along-slab geotherm model allows rate-and-state friction to predict the seismogenic zone depth limit for any given subduction zone (Fig. S9c).

In the Moho control model, if the megathrust is too cold and reaches the overriding plate Moho before the rate-and-state friction depth limit, then

mantle wedge processes end the seismogenic zone. The hypothesized mechanism is that fluids released from the slab combine with ultramafics from the overriding plate mantle to form velocity-strengthening serpentine minerals, along with talc and brucite, which may also be aseismic (Peacock and Hyndman, 1999). These minerals then prevent earthquake nucleation. While not emphasized in the initial Moho control studies (e.g., Oleskevich et al., 1999), the intersection of the subducting plate and Moho is not a sharp boundary and instead a complicated assemblage of sediments, crust, and mantle formed by erosion and underplating (Angiboust et al., 2022). Thus, we consider a $\pm$10 km depth range around the Moho.

3.2. Assessing Model Performance

As a first-order test on whether earthquake nucleation is temperature controlled via the rate-and-state model, we plot the temperature predicted by both thermal models at the observed seismogenic depth limit for each subduction zone and compare it to the rate-and-state predictions for each rock type: 350°C for granite, 510°C for gabbro, and 400°C for shale (Fig. 2c, d), with $\pm$25°C uncertainty for each rock type, following Oleskevich et al. (1999).

As seen in Fig. 2, the seismogenic depth limit is not controlled by a single temperature and is remarkably constant regardless of slab temperature (Heuret et al. (2011): mean=50$\pm$8.5 km; Slab2: mean=45$\pm$6.2 km). For both thermal models and both observational sets, the colder granite and shale limits perform better than the warmer gabbro, with 3-4, 1-2, and 0-1 subduction zones in the granite, shale, and gabbro ranges, respectively. For most subduction zones, the megathrust is too cold for rate-and-state friction to explain the lack of seismicity below $\sim$50 km, with $\geq$9 subduction zones below the 325°C lower bound for granite. Subduction zones do not scatter around a single temperature or rock type, and thus rate-and-state friction temperature control, or in fact, any process that is purely temperature controlled, cannot explain all observed depth limits at once. Increasing thermal model temperature, either by 200°C to better match petrological estimates, or via an overall increase in shear heating at $\mu'_{sh} = 0.12$, does not remove this temperature dependence (Fig. S3).

In the Moho control model, for subduction zones at <350°C, seismogenesis should stop when the megathrust intersects with the mantle wedge. However, of these $\geq$9 zones, only Northern Chile or Hikurangi fall within $\pm$10 km of the overriding plate Moho (Fig. 2e, f). The discrepancy is the

largest for oceanic-oceanic subduction zones (i.e., Izu-Bonin, Aleutians, Kermadec, and Mariana) where the inter-plate earthquakes occur ∼40 km deeper than the overriding plate Moho.

When we combine both criteria of the Moho control model, we find that it performs poorly: depending on the choice of thermal model and seismicity catalog, only between 1 and 4 out of 17 subduction zones are explained by this criterion (Fig. 2g, h), corresponding to an average failure rate of 87% across all four cases. The percentage increases to 89% when considering only well-constrained subduction zones, defined by the number of thrust earthquakes used to calculate the down-dip limit (Supplementary Material). In addition, only one zone is fit when thermal model shear heating increases and no zones are fit when geotherms are adjusted to match petrological estimates (Fig. S3).

Our analysis clearly shows that the Moho control model is insufficient to explain subduction seismogenic zone depth limits. The overriding plate Moho fails to demarcate the depth limit in cold subduction zones, and while, as a group, warm subduction zones are encompassed by the 350±25 to 510±25°C range, there exists no clear single temperature at which a transition from velocity-weakening to velocity-strengthening friction can explain the downdip limit of observed seismicity.

4. Frictional-Viscous Transition Model

4.1. Model Background

We model the FVT depth along the megathrust as the intersection of Byerlee's rule for frictional sliding and a viscous creep strength envelope (Fig. 1b), in order to identify mechanisms that best match observed depth limits and existing constraints on the strength of the megathrust.

4.1.1. Frictional Failure

To directly compare frictional and viscous strength, we express both failure criteria in terms of differential stress. As shown in Supplementary Material, the frictional failure criterion becomes

$$\sigma_f = \frac{2\mu'}{\sqrt{1+(\mu')^2}}\rho g z, \tag{3}$$

where μ' is the effective friction coefficient, ρ the overburden density, g acceleration due to gravity, and z depth. The effective friction coefficient accounts

for a reduction in effective normal stress due to pore pressure. This is expressed as

$$\tau = \mu(\sigma_n - P) = \mu'\sigma_n, \tag{4}$$

where μ is the friction coefficient, σ_n normal stress, and P pore pressure.

4.1.2. Power Law Creep

For power law creep, viscous strength is given by

$$\sigma_v = \left(\frac{\dot{\epsilon} d^m}{A f_{H_2O}^r}\right)^{1/n} \exp\left(\frac{Q}{nRT}\right), \tag{5}$$

where $\dot{\epsilon}$ is strain rate, d grain size, m a grain-size exponent, A an experimental pre-factor, f_{H_2O} water fugacity, r the water fugacity exponent, n the stress exponent, Q activation energy, R the ideal gas constant, and T temperature (Condit et al., 2022). We take $\dot{\epsilon}$ to be uniaxial strain rate (hereinafter referred to as strain rate) converting between shear strain rate ($\dot{\gamma}$) as needed using

$$\dot{\epsilon} = \dot{\gamma}/\sqrt{3} \tag{6}$$

(Paterson and Olgaard, 2000; French and Condit, 2019).

Experimental results for power law creep are separated into the dislocation and diffusion creep regimes and are analyzed separately for each mineral. Grain size controls which regime is the weakest and thus takes up plate motion.

Plate motion is accommodated by viscous deformation when it takes less differential stress to viscously deform the subduction channel than it does to accommodate relative plate motion through frictional failure. Thus, the FVT depth is located where $\sigma_f = \sigma_v$. Setting Eq. 5 equal to Eq. 3 allows us to solve for the depth of this transition as,

$$z = C_1 \exp\left(\frac{C_2}{T(z)}\right) \tag{7}$$

where

$$C_1 = \frac{\sqrt{1 + (\mu')^2}}{2\mu'\rho g}\left(\frac{\dot{\epsilon} d^m}{A f_{H_2O}^r}\right)^{1/n} \text{ and } C_2 = \frac{Q}{nR}. \tag{8}$$

where $T(z)$ is the temperature set by the along-slab geotherm (e.g., Fig. S9a). We solve for z numerically using the MATLAB root-finding function **fzero** (Brent, 2013; Forsythe et al., 1977).

4.1.3. Low-Temperature Plasticity

To define the viscous creep strength of LTP, we use the general form

$$\dot{\epsilon} = A\left(\frac{\sigma_v}{\mu_s}\right)^r \exp\left[\frac{-Q}{RT}\left(1-\left(\frac{\sigma_v}{\sigma_p}\right)^p\right)^q\right], \tag{9}$$

where A is an experimental pre-factor that can include terms such as water fugacity (Katayama and Karato, 2008), μ_s the shear modulus (Burdette and Hirth, 2022), r arises from the stress dependence of dislocation density, σ_p is the Peierls stress, and p and q depend on the barriers that dislocations must overcome during creep (Burdette and Hirth, 2022; Frost and Ashby, 1982). However, unlike power law creep, there is no closed form solution for σ_v. Thus, we invert Eq. 9 for $\sigma_v(z)$ and solve for z that satisfies $\sigma_v(z) = \sigma_f(z)$ (Eq. 3).

4.2. Applying the Model

4.2.1. Lithologies Considered

We focus on quartz, feldspar, and olivine as all three have published experimental flow laws for dislocation creep, diffusion creep, and LTP and are therefore directly comparable (Table 1). In addition, we analyze antigorite (serpentine) and talc LTP. Antigorite power law creep is excluded as the only published power law parameters were impacted by experimental issues (Hilairet et al., 2007; Burdette and Hirth, 2022; Shao et al., 2021). In the subduction setting, significant fluid is released during prograde metamorphism and porosity collapse (van Keken et al., 2011), thus we consider a hydrated or wet olivine. For LTP we also present a dry olivine case as it highlights the role of Peierls stress in controlling LTP strength. Our analysis does not include pressure solution creep, even though it is prevalent in the exhumed subduction zones record (Oncken et al., 2022), as pressure solution creep is sensitive to the length scale over which diffusion is occurring, and this can vary from micrometer-scale grain boundaries to km-scale fracture networks (Gratier et al., 2013), making experimental constraints challenging.

These experimental results constrain all FVT parameters except the overburden density, strain rate, and effective friction coefficient. We take $\rho = 2900$ kg/m^3 as a constant intermediate value for the overburden from overriding oceanic versus continental lithosphere. For the effective friction coefficient, we test $\mu' = 0.03 - 0.6$, with an end-member weak megathrust inferred from heat flow as a lower bound (Gao and Wang, 2017, 2014) and

Byerlee's friction as an upper bound (Byerlee, 1978). We plot $\mu' = 0.2$ as an example value, representing phyllosilicate fault gouge (Collettini et al., 2019). As discussed later, a reduced upper bound of $\mu' < 0.1$ is justifiable based on heat flow and force balance arguments. However, we start with a wider "plausible" range to evaluate model misfit more completely.

For strain rates, we calculate a geologically reasonable range. The full width of the megathrust fault zone is ∼100-350 m with creep occurring in strands ∼5-35 m thick (Rowe et al., 2013). Thus, the active deformation width spans three orders of magnitude and its true thickness at any point depends on the number of coeval creeping strands. Taking plate convergence rates between $10 - 100$ mm/yr and considering active deformation zones between $5 - 350$ m gives $\dot{\gamma}$ spanning $6.3 \times 10^{-10} - 9.1 \times 10^{-13}$ 1/s. Converting to uniaxial strain rate $\dot{\epsilon}$ gives upper and lower bounds of 3.7×10^{-10} and 5.2×10^{-13} 1/s, respectively, with a mean of 1.4×10^{-11} 1/s.

4.2.2. Forward Modeling and Inverting for Optimal Parameters

For the set of 17 subduction zone depth limits from Heuret et al. (2011), we run FVT forward models for all combinations of creep mechanism, thermal model with shear level of $\mu'_{sh} = 0.03$ (vK11m and WW09m), strain rate (5.2×10^{-13}, 1.4×10^{-11}, 3.7×10^{-10} 1/s) and effective friction coefficient (0.03, 0.2, 0.6) (Figs. S10, S11, S12, S13). For each thermal model and creep mechanism, the range of strain rates and friction coefficients determines the deepest and shallowest FVT predictions (deepest: $\mu' = 0.03$, $\dot{\epsilon} = 3.7 \times 10^{-10}$ 1/s; shallowest: $\mu' = 0.6$, $\dot{\epsilon} = 5.2 \times 10^{-13}$ 1/s) (Fig. 3). By plotting predicted depths for all $\dot{\epsilon}$ and μ', we visually identify a subset of mechanisms for which the observed depth limits are within the predicted range (e.g., Fig. 4a). These mechanisms are quartz dislocation creep and wet olivine, antigorite, and talc LTP (Table 2). For all other creep mechanisms, the observed depths fall outside of the estimated range, indicating that it is not geologically realistic for that mechanism to explain observations (e.g., Fig. 4b). Repeating this analysis for Slab2 observations and with the exclusion of poorly constrained subduction zones does not change which mechanisms are within the geologically realistic range (Table S4).

For the creep mechanisms that do cover the observations we carry out a grid-search inversion. For quartz dislocation creep we use a grid resolution of 50 by 51 between the upper and lower limits of effective friction coefficient and strain rate, respectively (Figs. 5, S14). We do the same for the LTP mechanisms with a higher grid search resolution of 100 by 101 (Figs. S15,

S16, wet olivine; Figs. 6, S17, antigorite; Figs. 7, S18, talc). In addition to inverting with Heuret et al. (2011) depth limits, we consider Slab2 and the case where poorly constrained subduction zones are removed (Table S4, Fig. S7). However, results do not meaningfully differ between each dataset, and for simplicity we focus on the complete Heuret et al. (2011) dataset.

Since laboratory parameters and their extrapolation to natural conditions are subject to large uncertainties and, as discussed later, power law creep fits observations poorly, it is worth asking if a hypothetical power law rheology could fit the data. To this end, we carry out an unconstrained grid-search inversion over lumped parameters C1 and C2. Although C1 and C2 are not constrained to an existing experimental creep mechanism, we limit them to plausible ranges of their constituent parameters (Supplementary Material).

5. Results

5.1. Power Law Creep

With the exception of quartz dislocation creep, power law creep mechanisms do not fit observed depth limits within their plausible effective friction coefficient and strain rate ranges (Fig. S10c, d, albite dislocation creep; Fig. S11c, d, albite diffusion creep; Fig. S10e, f, wet olivine dislocation creep; Fig. S11e, f, wet olivine diffusion creep; Fig. S11a, b, quartz diffusion creep).

As a whole, these mechanisms predict limits 20-40 km deeper than observations for all but the warmest subduction zones. The resultant minimum misfits range between 17.0-33.0 km (Table 2). This depth overprediction is due to the creep mechanisms being too strong and requiring higher temperatures associated with deeper depths in order to become weaker than frictional failure. The constant predicted depth of $\sim$80 km seen for many subduction zones is due to the modeled FVT falling within the rapid temperature increase associated with the maximum depth of decoupling (Wada and Wang, 2009).

Quartz dislocation creep performs better, encompassing the observed depth limits as a whole (Fig. 5a, Fig. S14a). The grid-search inversion for a best-fitting friction coefficient and strain rate reduces misfit to a minimum of 11.3 km for thermal model vK11m and 14.1 km for thermal model WW09m (Fig. 5b, Fig. S14b). However, it is apparent by visual inspection that these best-fit models match the average temperature subduction zone depth limits while predictions are too deep for cold ones and too shallow for warm ones. We quantitatively show this with residual analysis, i.e. by fitting a linear

regression to predicted depth against model residual (predicted depth minus observed depth) (Figs. 8b, S20a). The fits for both vK11m and WW09m have positive slopes, $R^2 > 0.7$, and they intersect a residual of ∼0 km roughly in the center of the predicted depth range (Table 2). This observation confirms that model error is correlated with the predicted depth and since variation in predicted depth between subduction zones is only a function of temperature, we conclude that quartz dislocation creep is too temperature sensitive. This analysis also highlights the importance of analyzing across the global subduction system. For example, quartz dislocation creep fits Nankai alone well and the overall misfit is only apparent when all 17 subduction zones are analyzed.

Increasing thermal model shear heating to $\mu_{sh} = 0.12$ weakens viscous creep, thus each mechanism fits the observed depths at a lower effective friction coefficient (e.g., Fig. S4). This weakening allows albite dislocation and diffusion to fit observations for $\mu' \leq 0.6$ (Table S2). However, albite misfit, residual slope, and residual R^2 are ∼16 km, ∼0.8, ∼0.8, respectively, showing albite does not offer improved data fit or reduced temperature sensitivity.

We use the unconstrained grid search inversion to conclusively confirm that any power law mechanism needs to be temperature insensitive to fit the observed depth limits. The unconstrained inversion reduces misfit to 5.9 km for thermal model vK11m and 7.2 km for thermal model WW09m (Figs. S5, S6), but requires activation energies of <20 kJ/mol, an extremely low value, an order of magnitude smaller than lab-reported activation energies (Table 1).

The source of this temperature oversensitivity can be seen by comparing the example viscous strength curves for quartz dislocation creep (Fig. 3a) and wet olivine LTP (Fig. 3b). Both curves are given by $\sigma_d(T(z))$ (Eqs. 5, 9). However, $\sigma_d(T(z))$ is vertical for wet olivine LTP while it is near horizontal for quartz dislocation creep. The horizontal envelopes result in a much larger spread of predicted FVT depths when intersected by the frictional failure criterion.

5.2. Low-Temperature Plasticity

The range of depths predicted for wet olivine, antigorite, and talc LTP encompass the observed seismogenic limits (Figs. S15a, S16a, wet olivine; Figs. 6a, S17a, antigorite; Figs. 7a, S18a, talc). The predicted FVT depths for all LTP mechanisms appear by visual inspection to be less temperature sensitive with flatter slopes across all subduction zones (e.g., Fig. 8a), consistent with the relatively constant observed seismogenic depths. However, dry

olivine, quartz, and plagioclase LTP are all too strong and predicted depth limits are too deep for nearly all observations (Fig. S12a, b, dry olivine; Fig. S13a, b, quartz; Fig. S13c, d, plagioclase). Thus, none of these mechanisms cover all the observed depth limits and minimum misfits vary from 12.9 to 26.9 km (Table 2).

The ability of wet olivine, antigorite, and talc to encompass the observed depth limits within the plausible friction coefficient and strain rate bounds is due to their lower Peierls stress of <3 GPa, in comparison to quartz, plagioclase, and dry olivine which have Peierls stress ≥4 GPa (Table 1). The Peierls stress sets the stress requirement to glide a dislocation at 0°K (Eq. 9). Thus, lowering Peierls stress weakens the mechanism overall and brings the FVT predictions closer to the observed depth limits. The lab-constrained grid-search inversion minimum misfits for wet olivine, antigorite, and talc are very low (Table 2). The wet olivine has a minimum misfit of 5.6 and 6.7 km for thermal model vK11m and WW09m (Figs. S15b, S16b), antigorite a misfit of 6.5 and 9.9 km (Fig. 6b, Fig. S17b), and talc a misfit of 5.6 and 6.7 (Fig. 7b, Fig. S18b). Residual slopes are low for all lithologies, but wet olivine and talc in particular, as confirmed visually by the random scatter of residuals in stark contrast to quartz dislocation (Fig. 8, Table 2).

The lab-constrained wet olivine, antigorite, and talc LTP mechanisms cases perform better than any power law creep mechanism, both in terms of misfit and residual slope. Furthermore, the misfits are on the same order as those from the unconstrained power law inversion (∼6-7 km), indicating that no hypothetical set of power law parameters offers an improvement over the LTP model with a low Peierls stress (<3 GPa). Lab-constrained LTP already captures the correct temperature sensitivity and does not require activation energies of <20 kJ/mol.

At a shear heating of $\mu'_{sh} = 0.12$, LTP still fits the observations better than power law creep. As with power law creep, the predicted depths shallow (e.g., Fig. S4), and the forward models for the $\mu' = 0.6$ friction upper limit approach observations. Minimum misfit decreases by 45% for quartz, plagioclase, and dry olivine LTP. However, quartz and plagioclase remain too strong and dry olivine only overlaps observations at $\mu' = 0.6$ (Table S2).

6. Discussion

6.1. Fault Strength

A clear finding of this work is that the downdip limit of the seismogenic zone is remarkably constant across warm and cold subduction zones, implying that temperature does not exert a first-order control, as typically assumed. Our more formal comparison of flow laws confirms that the observed earthquake depths are best explained by a frictional-viscous transition in which the viscous mechanisms have low temperature sensitivity. However, our grid search inversions present significant trade-offs between parameters: in particular, the predicted seismogenic depth limit is controlled by the relative strength between frictional sliding and viscous creep, and not by their absolute values. That is, slow strain rates with low friction coefficients produce similar depth limit predictions as fast strain rates with high friction coefficients (e.g., Fig. 3). Therefore, we consider fault strength as an external constraint to analyze the FVT model results, focusing on thermal model vK11m as the minimum misfit for vK11m is lower than WW09m.

Megathrust fault strength is constrained by the force balance required to support mountain belts (Lamb, 2006) and the effective friction levels required to match forearc heat flux data (England, 2018). Reported effective friction coefficients are consistently < 0.1 (England, 2018; Gao and Wang, 2014), and given this is much less than Byerlee's friction of 0.6, we refer to $\mu' < 0.1$ as a weak fault.

At their minimum misfit levels, wet olivine and antigorite LTP are too strong, while talc LTP and quartz dislocation allow for a weak fault. The low-misfit region (11.4 km contour) for quartz dislocation creep occurs at $\mu' < 0.1$ for strain rates $<\sim 10^{-11.25}$ 1/s (Fig. 5c). However, the low-misfit regions for both wet olivine LTP and antigorite LTP never cross to $\mu' < 0.1$ (Fig. S15c, wet olivine LTP, 5.7 km contour; Fig. 6c, antigorite LTP, 6.7 km contour). Both mechanisms sit between $\mu' = 0.2 - 0.33$, requiring peak shear strengths > 250 MPa. However, if we allow both LTP mechanisms an 11.4 km misfit, making comparison to quartz dislocation equal, antigorite LTP does have a weak fault for strain rates $<\sim 10^{-10.6}$ 1/s. Increasing shear heating to $\mu'_{sh} = 0.12$ brings μ' closer to 0.1, especially for antigorite, but both remain > 0.1 at their minimum misfit (Fig. S4c-f). Talc LTP has a Peierls stress an order of magnitude smaller than all other lithologies, thus its minimum misfit region (5.7 km contour) falls between $\mu' = 0.04 - 0.05$

at $60 - 70$ MPa, with the full 11.4 km quartz comparison contour falling at $\mu' < 0.085$.

Due to its low temperature dependence and misfit ($\sim$6 km), we favor LTP as the appropriate mechanism over quartz dislocation creep. However, only talc LTP meets the weak fault criteria. This strength mismatch for antigorite LTP appears in existing work. Along the Chilean margin and Japan trench, Wang et al. (2025) and Wang and He (2025) concluded that the transition from antigorite frictional failure to LTP, not the overriding plate Moho, controls the seismogenic depth limit. However, LTP strength must be reduced by 50% to match the observed depth limits at $\sim$50 km and keep the megathrust weak with $\mu' = 0.04 - 0.06$ (c.f., Fig. 6b, Wang et al., 2025). This reduction is justified by leaning on antigorite as the strongest mineral in the shear zone and thus a 100% antigorite LTP flow law is an upper bound, and a 50% scaled-antigorite reduction better captures the bulk fault rheology. Our work shows that the global subduction system requires a reduction in LTP strength and that talc LTP meets this requirement.

6.2. Megathrust Lithology

Of the minerals we model, only olivine is not a matrix-forming mineral in the subduction rock record. Quartz and feldspar are present in exhumed subduction zones (e.g., as metasedimentary schist) (Condit et al., 2022; Kotowski and Behr, 2019). Any olivine that is entrained in the subduction shear zone from the mantle is metamorphosed to serpentine (antigorite) and talc in the presence of slab-derived fluids (Peacock and Hyndman, 1999), confirmed by serpentine and talc presence in exhumed subduction rocks (French and Condit, 2019; Easthouse et al., 2025). Serpentine and talc are also likely to host deformation as serpentine is mechanically weaker than olivine, and talc is $\sim$3-4 times weaker than other phyllosilicates, including serpentine (Escartin et al., 2001; Boneh et al., 2023). In addition, talc is stable at the pressure and temperature conditions of the full subduction seismogenic zone (Pawley and Wood, 1995).

We have shown that both the antigorite and talc LTP models predict observed depth limits extremely well ($\sim$6 km misfit), and talc allows for weak megathrusts ($\mu' < 0.1$) across the global subduction system. Talc is an ideal candidate to control the downdip limit as it is found in the majority of exhumed subduction zones (Easthouse et al., 2025). In fact, at the advent of the Moho control model, talc was theoretically shown to form in the mantle

wedge and hypothesized to play a role in the downdip limit due to being a weak phyllosilicate (Peacock and Hyndman, 1999).

Regardless of talc prevalence, antigorite and talc LTP are both just candidate mechanisms and the key takeaway is that any mechanism that explains the observed depth limits must be extremely temperature insensitive, fit ∼50 km depth, and be weak enough to allow for a fault with $\mu' < 0.1$. For example, novel low-Q power-law mechanisms such as nanometric flow (Sun and Pec, 2021), improved constraints on pressure solution creep (e.g., Fisher and Hirth, 2024), or LTP experiments with different minerals, could match the data equally well.

Here we test the same monomineralic flow law, friction coefficient, and strain rate across the 17 subduction zones as our goal is to test the simplest models first before adding free parameters. This universality is a strong assumption, as variation in pressure-temperature path between subduction zones results in different mineral assemblages (Condit et al., 2020); however, the low misfits in our analysis indicate that the data does not require lithological differences across subduction zones. It is possible that weak and temperature-insensitive flow is common across rock types, and the universality of the mechanism itself controls the downdip limit of the seismogenic zone globally, not the universality of a specific lithology like talc. Regardless of how realistic a monomineralic frictional-viscous transition model is, it is remarkable that there is no need to invoke significant rheological differences to fit the observed data to a ∼6 km misfit.

7. Conclusion

In this work we revisit the physical mechanisms controlling the downdip limit of the subduction seismogenic zone by integrating newer earthquake observations, thermal models, and lab friction experiments. By analyzing across the global system, we are able to rule out mechanisms that may explain earthquake depths for any particular region, but do not generalize beyond an individual subduction zone. Our main findings are as follows:

- Global seismogenic zone depth limits do not occur at a single temperature; in fact, they span over ∼250°C with many occurring at <350°C. Therefore, a temperature controlled change from rate-and-state velocity-weakening to velocity-strengthening friction cannot explain the observed depth limits.

- The hypothesis that the seismogenic depth limit is controlled by the shallowest between the upper plate Moho and the 350°C isotherm is not supported by the data: across 17 subduction zones, two observed depth limit data sets, and two independent thermal models, the Moho control model works only 9 out 68 times, a 87% failure rate. For warm subduction zones 350°C is too cold and for cold subduction zones the overriding plate Moho is too shallow for either to control the megathrust seismogenic zone depth limit.

- Any candidate process to explain the observed depths limits must be extremely temperature insensitive and overall predict a relatively constant depth ($\sim$50 km) for all subduction zones.

- Laboratory constrained power law creep mechanisms (quartz dislocation and diffusion, albite dislocation and diffusion, and olivine dislocation and diffusion) with activation energies $\geq$135 kJ/mol are too temperature sensitive to explain the observed seismogenic depth limit as a frictional-viscous transition. An activation energy of $\leq$20 kJ/mol can fit observed depth limits to a misfit of $\sim$6 km, but this value is significantly lower than most lab reported values, suggesting that the onset of power law creep is not the appropriate viscous mechanism to arrest seismogenesis.

- Wet olivine, antigorite, and talc low-temperature plasticity are appropriately temperature insensitive and are able to fit observed depth limits to a misfit of $\sim$6 km using lab-constrained parameters. Wet olivine and antigorite require effective friction coefficients between 0.2-0.33 with mean peak shear strength of >250 MPa, while talc allows for a coefficient <0.1 and shear strengths on the order of tens of MPa, more consistent with external constraints for a weak megathrust.

- Talc is found in the majority of exhumed subduction zones and thus could control the downdip limit of megathrust seismogenisis.

8. CRediT authorship contribution statement

Liam Moser: Conceptualization, Methodology, Software, Validation, Formal analysis, Investigation, Data curation, Writing - Original Draft, Writing - Review & Editing, Visualization. **Matěj Peč:** Conceptualization, Writ-

ing - Review & Editing. **Camilla Cattania:** Conceptualization, Methodology, Software, Validation, Formal analysis, Writing - Review & Editing, Supervision.

9. Supplementary material

Supplementary material is available with the online version of this article. Our frictional-viscous transition inversion code is publicly available (Moser et al., 2025) and can be used to evaluate how well other flow laws, current and future, can predict the observed megathrust seismogenic zone depth limits.

10. Acknowledgments

Thank you to Hannah Shabtian for an insightful discussion on talc low-temperature plasticity and for providing experimental results. Thank you to Juan Pablo Canales for his continued support of Liam Moser working on this project. This work was supported by the J.H. and E.V. Wade Fund and a National Science Foundation CAREER award to Camilla Cattania (Grant 2339556).

Table 1: Power law and LTP parameters used in forward models. Quartz dislocation creep, albite dislocation creep, and albite diffusion creep are taken from the Condit et al. (2022) compilation, with quartz dislocation creep specifically from Hirth et al. (2001) and albite dislocation and diffusion creep specifically from Offerhaus et al. (2001). Quartz diffusion creep is from Rutter and Brodie (2004). Wet olivine dislocation and diffusion creep are from Hirth and Kohlstedt (2003). Quartz and plagiocase LTP are from Sly et al. (2023). Dry olivine, wet olivine, antigorite, and talc LTP are from Mei et al. (2010), Katayama and Karato (2008), Burdette and Hirth (2022), and Shabtian and Hirth (2025), respectively. For quartz, plagioclase, and wet olivine LTP different Peierls stress cases are published that depend on barrier parameters p and q as well as the conversion from indentation hardness to yield stress. We take the minimum Peierls stress, allowing for the weakest fault.

Power law mechanism	A	Q (kJ/mol)	n	d (μm)	m	f_{H_2O} (MPa)	r
Quartz dislocation	$10^{-11.2}$	135	4	n/a	0	280[a]	1
Quartz diffusion	0.4	220	1	15	2	n/a[b]	n/a[b]
Albite dislocation	$10^{3.4}$	332	3	n/a	0	n/a	0
Albite diffusion	$10^{3.9}$	193	1	15	3	n/a	0
Wet olivine dislocation	1600	480	3.5	n/a	0	280[c]	1.2
Wet olivine diffusion	2.5×10^{7}	375	1	7.5[d]	3	280[c]	1
LTP mechanism	A	Q (kJ/mol)	σ_p (MPa)	μ_s (MPa)	r	p	q
Quartz	8.23×10^{-6}	607	5.70×10^{3}	n/a	2	1	1
Plagioclase	8.13×10^{-6}	650	4.00×10^{3}	n/a	2	1	1
Dry olivine	1.4×10^{-7}	320	5.9×10^{3}	n/a	2	1	0.5
Wet olivine	10^{8}	518	1.58×10^{3}	n/a	1.4	1	1
Antigorite	exp(-0.624)	86.3	2.42×10^{3}	35×10^{3}	2	1.18	1
Talc	exp(8.55)	120	330	22×10^{3}	2	1.5	1

Constants: $g = 9.8$ m/s^2 and $R = 8.314472$ J/K$\times$mol.
[a]Pitzer and Sterner (1995), [b]water fugacity accounted for in pre-factor (A)
[c]Set to match quartz dislocation
[d]Set to half albite grain size (c.f., Fig. 7a Hirth and Kohlstedt (2003))

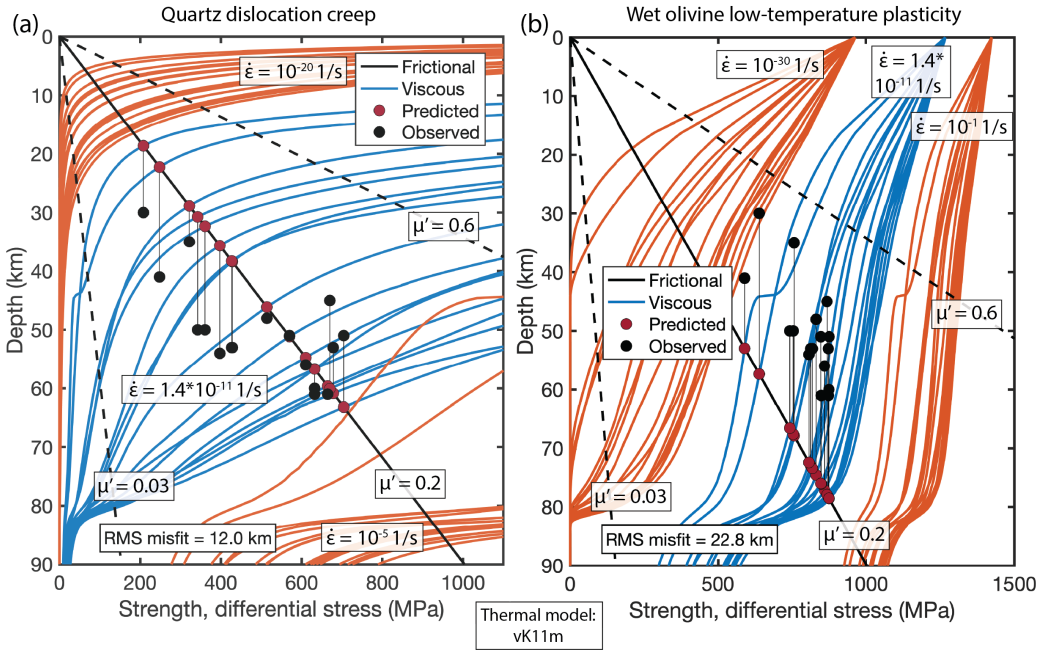

Figure 3: Examples of the FVT forward modeling procedure for (a) quartz dislocation creep and (b) wet olivine LTP. Blue lines are viscous strength curves for all 17 subduction zones at the mean geologic strain rate. These lines are intersected with the black frictional failure strength line to give predicted FVTs (red circles), with $\mu' = 0.2$ shown as an example, not as the best fitting or most realistic coefficient. Vertical black lines connect each prediction to the observed depth limit (black circles) visualizing model misfit. Note that observed depth limits are plotted at the predicted FVT strength for visualization purposes, but they are not inherently tied to a specific fault strength. Orange lines are viscous strength curves at exaggerated strain rate bounds to show effect of increasing or decreasing strain rate on predicted FVT depth. Black dashed lines show the geologically plausible effective friction coefficient bounds for same purpose.

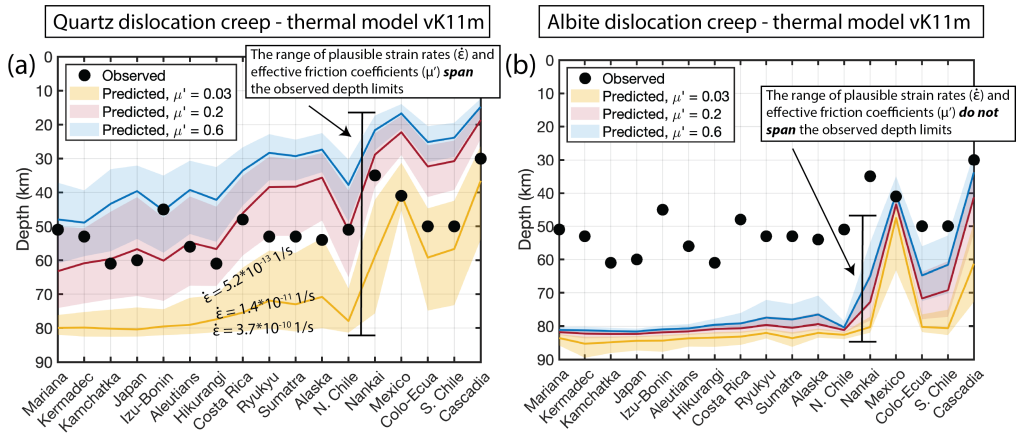

Figure 4: Examples of how the geologically plausible predicted FVT ranges can (a) span or (b) not span the observed depth limits depending on creep mechanism. Black circles are the observed seismogenic zone depth limits. Color denotes effective friction coefficient. Each colored patch is the range of predictions between the minimum and maximum strain rate of 5.2×10^{-13} and 3.7×10^{-10} 1/s and the solid lines denote the mean strain rate of 1.4×10^{-11} 1/s.

Table 2: Summary of FVT results by viscous creep mechanism. "Within bounds" denotes that the minimum misfit does not occur on the upper or lower bound of the geologically plausible parameter range and thus a grid search inversion is used to locate the minimum. "Residual slope" is the linear regression slope of predicted FVT depths against model residuals for the minimum misfit case. The best fitting mechanisms are bolded.

Creep mechanism	**Min. misfit (km) vK11m/WW09m**	**Within bounds**	**Residual slope**	**Residual R^2**
Quartz dislocation	11.3/14.4	yes/yes	0.62/0.69	0.72/0.82
Quartz diffusion	33.0/28.2	no/no	N/A	N/A
Albite dislocation	21.1/17.0	no/no	N/A	N/A
Albite diffusion	17.7/17.1	no/no	N/A	N/A
Wet olivine dislocation	30.0/25.1	no/no	N/A	N/A
Wet olivine diffusion	31.1/26.2	no/no	N/A	N/A
Quartz LTP	26.9/23.2	no/no	N/A	N/A
Plagioclase LTP	19.0/17.7	no/no	N/A	N/A
Dry olivine LTP	13.3/12.9	no/no	N/A	N/A
Wet olivine LTP	5.6/6.6	yes/yes	-0.13/0.13	0.02/0.01
Antigorite LTP	6.5/9.9	yes/yes	0.35/0.59	0.25/0.57
Talc LTP	5.6/6.7	yes/yes	0.00/0.01	0.00/0.00

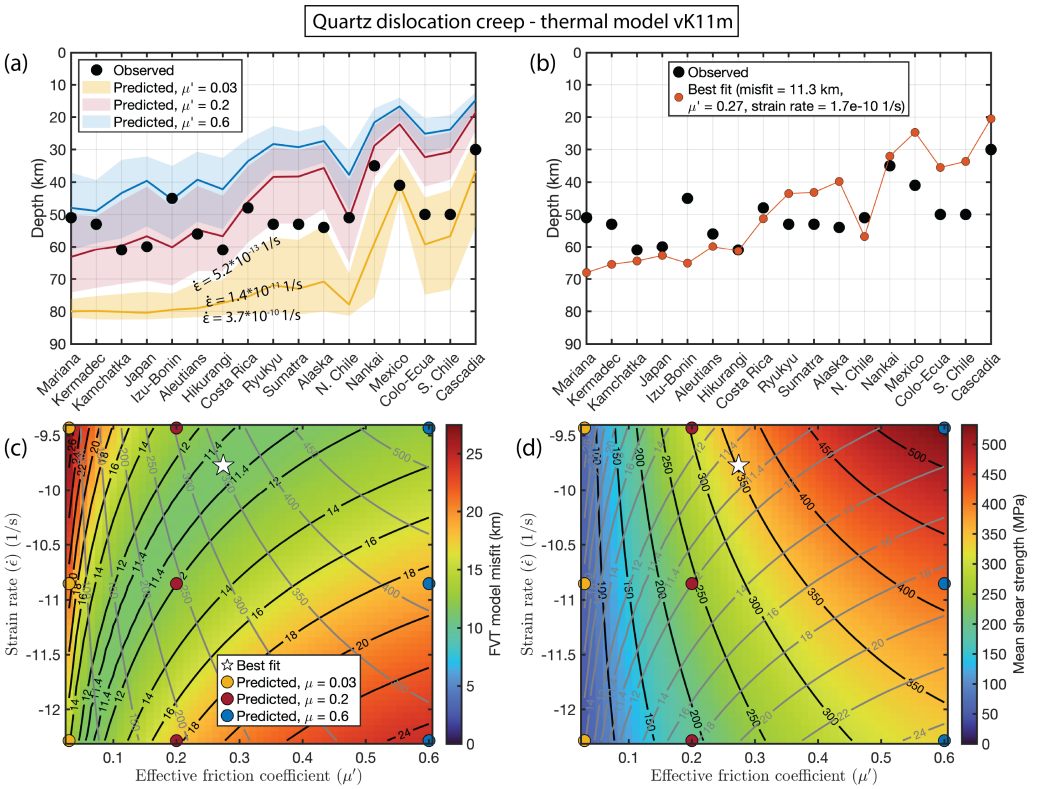

Figure 5: FVT inversion for quartz dislocation creep with thermal model vK11m. (a) Lab constrained forward models. (b) Best fitting model between $\mu' = 0.03 - 0.6$ and $\dot{\epsilon} = 5.2 \times 10^{-13} - 3.7 \times 10^{-10}$ 1/s. (c) Grid search with black lines as root-mean-square misfit contours. Gray contours are mean shear strength. White star denotes best fitting model shown in (b) and circles are parameters of forward models plotted in (a). (d) Same as (c) except for mean shear strength of all 17 subduction zones at the predicted FVT.

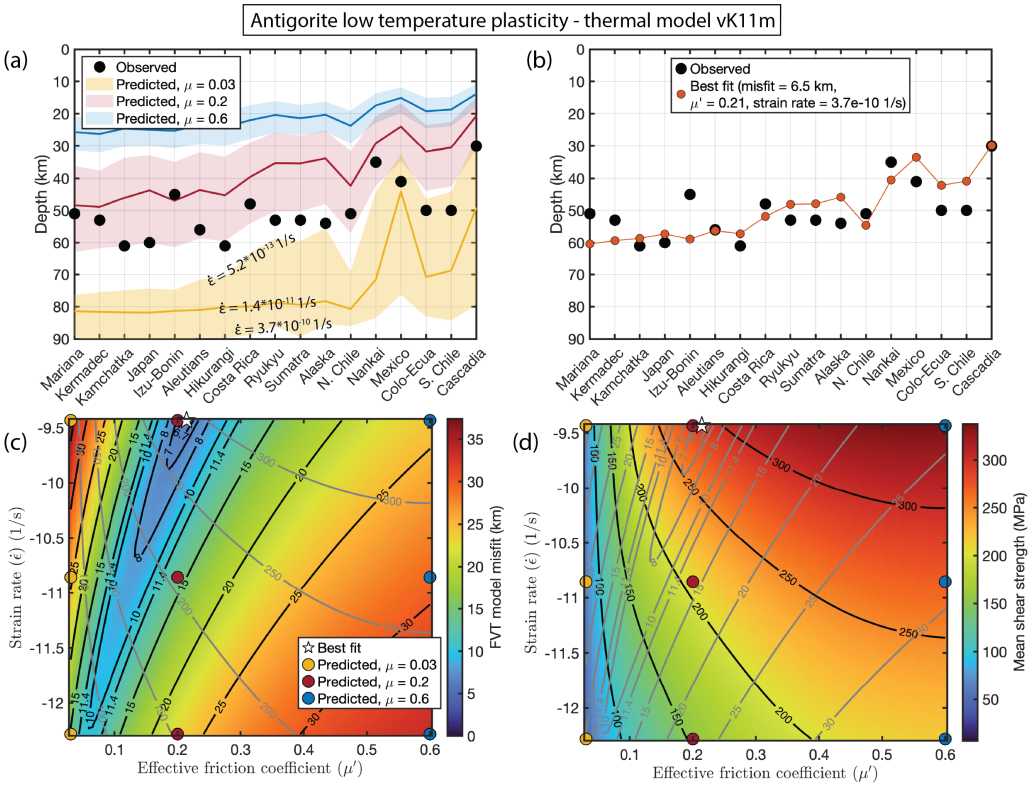

Figure 6: FVT inversion for antigorite LTP with thermal model vK11m. (a) Lab constrained forward models. (b) Best fitting model between $\mu' = 0.03 - 0.6$ and $\dot{\epsilon} = 5.2 \times 10^{-13} - 3.7 \times 10^{-10}$ 1/s. (c) Grid search with black lines as root-mean-square misfit contours. Gray contours are mean shear strength. White star denotes best fitting model shown in (b) and circles are parameters of forward models plotted in (a). (d) Same as (c) except for mean shear strength of all 17 subduction zones at the predicted FVT.

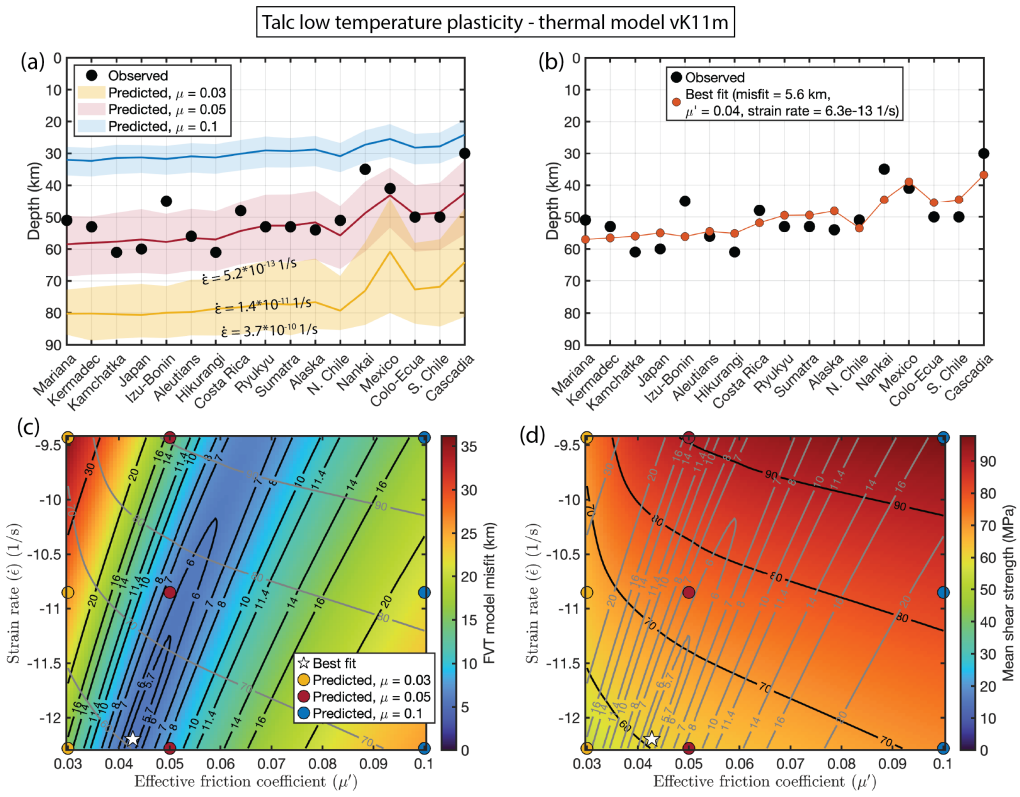

Figure 7: FVT inversion for talc LTP with thermal model vK11m. (a) Lab constrained forward models with $\mu' = 0.03$, 0.05, and 0.1 plotted due to talc weakness. (b) Best fitting model between $\mu' = 0.03 - 0.1$ and $\dot{\epsilon} = 5.2 \times 10^{-13} - 3.7 \times 10^{-10}$ 1/s. (c) Grid search with black lines as root-mean-square misfit contours. Gray contours are mean shear strength. White star denotes best fitting model shown in (b) and circles are parameters of forward models plotted in (a). (d) Same as (c) except for mean shear strength of all 17 subduction zones at the predicted FVT.

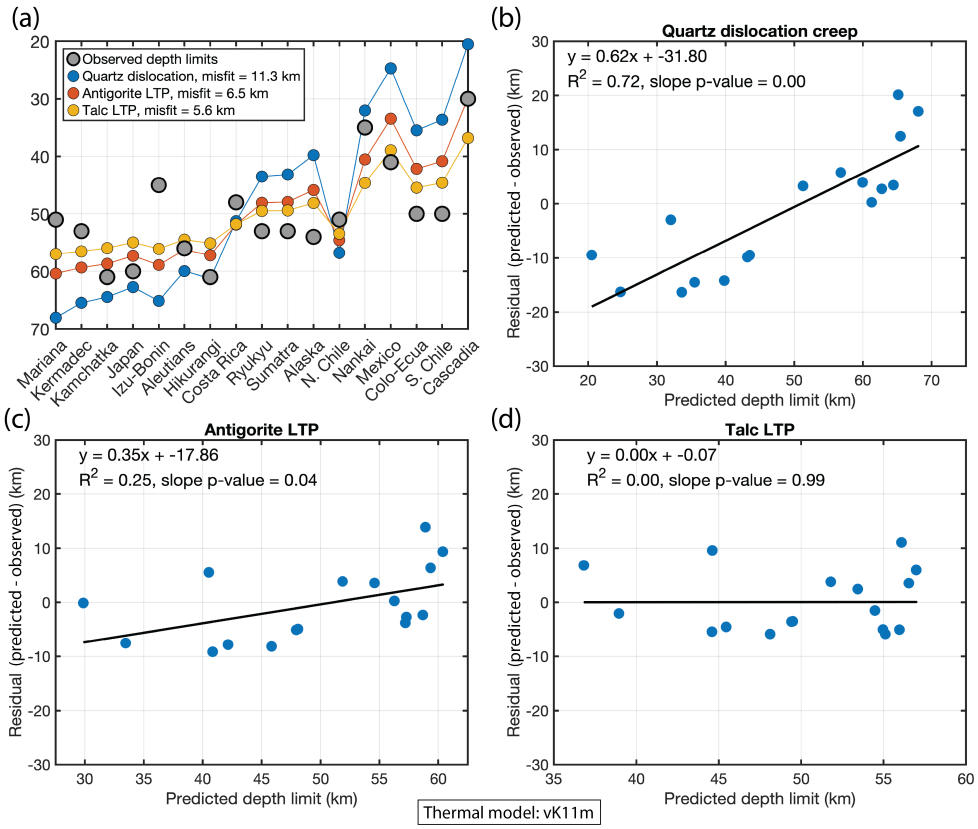

Figure 8: Residual analysis of predicted FVT from grid-search inversions. (a) Comparison of best fit models for quartz dislocation creep, wet olivine LTP, and antigorite LTP with residuals shown in (b), (c), and (d) respectively. Residual values are predicted minus observed. Each blue circle is a single subduction zone. A line is fit to the residuals to quantify the correlation between predicted depth and model misfit.

References

Aharonov, E., Scholz, C.H., 2019. The brittle-ductile transition predicted by a physics-based friction law. Journal of Geophysical Research: Solid Earth 124, 2721–2737. URL: https://doi.org/10.1029/2018JB016878.

Angiboust, S., Menant, A., Gerya, T., Oncken, O., 2022. The rise and demise of deep accretionary wedges: A long-term field and numerical modeling perspective. Geosphere 18, 69–103. URL: https://doi.org/10.1130/GES02392.1.

Blanpied, M., Marone, C., Lockner, D., Byerlee, J., King, D., 1998. Quantitative measure of the variation in fault rheology due to fluid-rock interactions. Journal of Geophysical Research: Solid Earth 103, 9691–9712. URL: https://doi.org/10.1029/98JB00162.

Boneh, Y., Pec, M., Hirth, G., 2023. High-pressure mechanical properties of talc: Implications for fault strength and slip processes. Journal of Geophysical Research: Solid Earth 128, e2022JB025815. URL: https://doi.org/10.1029/2022JB025815.

Brent, R.P., 2013. Algorithms for minimization without derivatives. Courier Corporation.

Burdette, E., Hirth, G., 2022. Creep rheology of antigorite: Experiments at subduction zone conditions. Journal of Geophysical Research: Solid Earth 127, e2022JB024260. URL: https://doi.org/10.1029/2022JB024260.

Byerlee, J., 1978. Friction of rocks. Rock friction and earthquake prediction , 615–626URL: https://linkspringer.com/book/10.1007/978-3-0348-7182-2.

Collettini, C., Tesei, T., Scuderi, M.M., Carpenter, B.M., Viti, C., 2019. Beyond byerlee friction, weak faults and implications for slip behavior. Earth and Planetary Science Letters 519, 245–263. URL: https://doi.org/10.1016/j.epsl.2019.05.011.

Condit, C.B., French, M.E., Hayles, J.A., Yeung, L.Y., Chin, E.J., Lee, C.T.A., 2022. Rheology of metasedimentary rocks at the base of the subduction seismogenic zone. Geochemistry, Geophysics, Geosystems 23, e2021GC010194. URL: https://doi.org/10.1029/2021GC010194.

Condit, C.B., Guevara, V.E., Delph, J.R., French, M.E., 2020. Slab dehydration in warm subduction zones at depths of episodic slip and tremor. Earth and Planetary Science Letters 552, 116601. URL: https://doi.org/10.1016/j.epsl.2020.116601.

Dieterich, J.H., 1979. Modeling of rock friction: 1. experimental results and constitutive equations. Journal of Geophysical Research: Solid Earth 84, 2161–2168. URL: https://doi.org/10.1029/JB084iB05p02161.

Dziewonski, A.M., Chou, T.A., Woodhouse, J.H., 1981. Determination of earthquake source parameters from waveform data for studies of global and regional seismicity. Journal of Geophysical Research: Solid Earth 86, 2825–2852. URL: https://doi.org/10.1029/JB086iB04p02825.

Easthouse, G., Hoover, W., Teng, F.Z., Condit, C., Pike, C., Wang, Z.Z., Berg, A., Wynn, P., Woods, L., Poulaki, E., 2025. Formation of talc in the subduction interface: Mg isotopes demonstrate mg loss over si gain. Geology 53, 398–403. URL: https://doi.org/10.1130/G52538.1.

Engdahl, E.R., van der Hilst, R., Buland, R., 1998. Global teleseismic earthquake relocation with improved travel times and procedures for depth determination. Bulletin of the Seismological Society of America 88, 722–743. URL: https://doi.org/10.1785/BSSA0880030722.

England, P., 2018. On shear stresses, temperatures, and the maximum magnitudes of earthquakes at convergent plate boundaries. Journal of Geophysical Research: Solid Earth 123, 7165–7202. URL: https://doi.org/10.1029/2018JB015907.

Erickson, B.A., Jiang, J., Barall, M., Lapusta, N., Dunham, E.M., Harris, R., Abrahams, L.S., Allison, K.L., Ampuero, J.P., Barbot, S., Cattania, C., Elbanna, A., Fialko, Y., Idini, B., Kozdon, J.E., Lambert, V., Liu, Y., Luo, Y., Ma, X., Best McKay, M., Segall, P., Shi, P., van den Ende, M., Wei, M., 2020. The community code verification exercise for simulating sequences of earthquakes and aseismic slip (seas). Seismological Research Letters 91, 874–890. URL: https://doi.org/10.1785/0220190248.

Escartin, J., Hirth, G., Evans, B., 2001. Strength of slightly serpentinized peridotites: Implications for the tectonics of oceanic lithosphere. Geology 29, 1023–1026. URL: https://doi.org/10.1130/0091-7613(2001)029<1023:SOSSPI>2.0.CO;2.

Fisher, D.M., Hirth, G., 2024. A pressure solution flow law for the seismogenic zone: Application to cascadia. Science Advances 10, eadi7279. URL: https://doi.org/10.1126/sciadv.adi7279.

Forsythe, G.E., Malcolm, M.A., Moler, C.B., 1977. Computer methods for mathematical computations. Prentice-hall. URL: https://dl.acm.org/doi/abs/10.5555/578659.

French, M.E., Condit, C.B., 2019. Slip partitioning along an idealized subduction plate boundary at deep slow slip conditions. Earth and Planetary Science Letters 528, 115828. URL: https://doi.org/10.1016/j.epsl.2019.115828.

Frost, H.J., Ashby, M.F., 1982. Deformation mechanism maps: The plasticity and creep of metals and ceramics. Pergamon press. URL: https://defmech.engineering.dartmouth.edu/.

Gao, X., Wang, K., 2014. Strength of stick-slip and creeping subduction megathrusts from heat flow observations. Science 345, 1038–1041. URL: https://doi.org/10.1126/science.1255487.

Gao, X., Wang, K., 2017. Rheological separation of the megathrust seismogenic zone and episodic tremor and slip. Nature 543, 416–419. URL: https://doi.org/10.1038/nature21389.

Gratier, J.P., Dysthe, D.K., Renard, F., 2013. The role of pressure solution creep in the ductility of the earth's upper crust. Advances in geophysics 54, 47–179. URL: https://doi.org/10.1016/B978-0-12-380940-7.00002-0.

den Hartog, S.A.M., Spiers, C.J., 2013. Influence of subduction zone conditions and gouge composition on frictional slip stability of megathrust faults. Tectonophysics 600, 75–90. URL: https://doi.org/10.1016/j.tecto.2012.11.006.

Hayes, G.P., Moore, G.L., Portner, D.E., Hearne, M., Flamme, H., Furtney, M., Smoczyk, G.M., 2018. Slab2, a comprehensive subduction zone geometry model. Science 362, 58–61. URL: https://doi.org/10.1126/science.aat4723.

He, C., Wang, Z., Yao, W., 2007. Frictional sliding of gabbro gouge under hydrothermal conditions. Tectonophysics 445, 353–362. URL: https://doi.org/10.1016/j.tecto.2007.09.008.

Heuret, A., Lallemand, S., Funiciello, F., Piromallo, C., Faccenna, C., 2011. Physical characteristics of subduction interface type seismogenic zones revisited. Geochemistry, Geophysics, Geosystems 12. URL: https://doi.org/10.1029/2010GC003230.

Hilairet, N., Reynard, B., Wang, Y., Daniel, I., Merkel, S., Nishiyama, N., Petitgirard, S., 2007. High-pressure creep of serpentine, interseismic deformation, and initiation of subduction. Science 318, 1910–1913. URL: https://doi.org/10.1126/science.1148494.

Hirauchi, K.i., Katayama, I., Uehara, S., Miyahara, M., Takai, Y., 2010. Inhibition of subduction thrust earthquakes by low-temperature plastic flow in serpentine. Earth and Planetary Science Letters 295, 349–357. URL: https://doi.org/10.1016/j.epsl.2010.04.007.

Hirth, G., Kohlstedt, D., 2003. Rheology of the upper mantle and the mantle wedge: A view from the experimentalists. Geophysical monograph-american geophysical union 138, 83–106. URL: https://doi.org/10.1029/138GM06.

Hirth, G., Teyssier, C., Dunlap, J.W., 2001. An evaluation of quartzite flow laws based on comparisons between experimentally and naturally deformed rocks. International Journal of Earth Sciences 90, 77–87. URL: https://doi.org/10.1007/s005310000152.

Horn, C., Skemer, P., 2023. Semi-brittle deformation of talc at the base of the seismogenic zone. Geophysical Research Letters 50, e2022GL102385. URL: https://doi.org/10.1029/2022GL102385.

Hyndman, R.D., Yamano, M., Oleskevich, D.A., 1997. The seismogenic zone of subduction thrust faults. Island Arc 6, 244–260. URL: https://doi.org/10.1111/j.1440-1738.1997.tb00175.x.

Katayama, I., Karato, S.i., 2008. Low-temperature, high-stress deformation of olivine under water-saturated conditions. Physics of the Earth and Planetary Interiors 168, 125–133. URL: https://doi.org/10.1016/j.pepi.2008.05.019.

van Keken, P.E., Hacker, B.R., Syracuse, E.M., Abers, G.A., 2011. Subduction factory: 4. depth-dependent flux of h2o from subducting slabs worldwide. Journal of Geophysical Research: Solid Earth 116. URL: https://doi.org/10.1029/2010JB007922.

van Keken, P.E., Wada, I., Abers, G.A., Hacker, B.R., Wang, K., 2018. Mafic high-pressure rocks are preferentially exhumed from warm subduction settings. Geochemistry, Geophysics, Geosystems 19, 2934–2961. URL: https://doi.org/10.1029/2018GC007624.

Kirby, S.H., Durham, W.B., Stern, L.A., 1991. Mantle phase changes and deep-earthquake faulting in subducting lithosphere. Science 252, 216–225. URL: https://doi.org/10.1126/science.252.5003.216.

Kotowski, A.J., Behr, W.M., 2019. Length scales and types of heterogeneities along the deep subduction interface: Insights from exhumed rocks on syros island, greece. Geosphere 15, 1038–1065. URL: https://doi.org/10.1130/GES02037.1.

Lamb, S., 2006. Shear stresses on megathrusts: Implications for mountain building behind subduction zones. Journal of Geophysical Research: Solid Earth 111. URL: https://doi.org/10.1029/2005JB003916.

Lay, T., Kanamori, H., Ammon, C.J., Nettles, M., Ward, S.N., Aster, R.C., Beck, S.L., Bilek, S.L., Brudzinski, M.R., Butler, R., DeShon, H.R., Ekström, G., 2005. The great sumatra-andaman earthquake of 26 december 2004. Science 308, 1127–1133. URL: https://doi.org/10.1126/science.1112250.

Liu, Y., Rice, J.R., 2009. Slow slip predictions based on granite and gabbro friction data compared to gps measurements in northern cascadia. Journal of Geophysical Research: Solid Earth 114. URL: https://doi.org/10.1029/2008JB006142.

Mei, S., Suzuki, A., Kohlstedt, D., Dixon, N., Durham, W., 2010. Experimental constraints on the strength of the lithospheric mantle. Journal of Geophysical Research: Solid Earth 115. URL: https://doi.org/10.1029/2009JB006873.

Molnar, P., Freedman, D., Shih, J.S., 1979. Lengths of intermediate and deep seismic zones and temperatures in downgoing slabs

of lithosphere. Geophysical Journal International 56, 41–54. URL: https://doi.org/10.1111/j.1365-246X.1979.tb04766.x.

Moore, D.E., Lockner, D., Ma, S., Summers, R., Byerlee, J., 1997. Strengths of serpentinite gouges at elevated temperatures. Journal of Geophysical Research: Solid Earth 102, 14787–14801. URL: https://doi.org/10.1029/97JB00995.

Moser, L., Cattania, C., Peč, M., 2025. Temperature insensitive viscous deformation limits megathrust seismogenesis. URL: https://doi.org/10.5281/zenodo.15351145.

Offerhaus, L., Wirth, R., Dresen, G., 2001. High-temperature creep of polycrystalline albite. Deformation Mechanisms, Rheology and Tectonics 124, 107–131. URL: https://cir.nii.ac.jp/crid/1370298757401021461.

Oleskevich, D., Hyndman, R., Wang, K., 1999. The updip and downdip limits to great subduction earthquakes: Thermal and structural models of cascadia, south alaska, sw japan, and chile. Journal of Geophysical Research: Solid Earth 104, 14965–14991. URL: https://doi.org/10.1029/1999JB900060.

Oncken, O., Angiboust, S., Dresen, G., 2022. Slow slip in subduction zones: Reconciling deformation fabrics with instrumental observations and laboratory results. Geosphere 18, 104–129. URL: https://doi.org/10.1130/GES02382.1.

Paterson, M., Olgaard, D., 2000. Rock deformation tests to large shear strains in torsion. Journal of structural Geology 22, 1341–1358. URL: https://doi.org/10.1016/S0191-8141(00)00042-0.

Pawley, A.R., Wood, B.J., 1995. The high-pressure stability of talc and 10 å phase: potential storage sites for h2o in subduction zones. American Mineralogist 80, 998–1003. URL: https://doi.org/10.2138/am-1995-9-1015.

Peacock, S.M., Bostock, M.G., 2024. Serpentinization of the forearc mantle wedge in subduction zones: Revisiting roy d. hyndman's seminal contributions 25 years later. Canadian Journal of Earth Sciences URL: tps://doi.org/10.1139/cjes-2024-0082.

Peacock, S.M., Hyndman, R.D., 1999. Hydrous minerals in the mantle wedge and the maximum depth of subduction thrust earthquakes. Geophysical Research Letters 26, 2517–2520. URL: https://doi.org/10.1029/1999GL900558.

Penniston-Dorland, S.C., Kohn, M.J., Manning, C.E., 2015. The global range of subduction zone thermal structures from exhumed blueschists and eclogites: Rocks are hotter than models. Earth and Planetary Science Letters 428, 243–254. URL: https://doi.org/10.1016/j.epsl.2015.07.031.

Pitzer, K.S., Sterner, S., 1995. Equations of state valid continuously from zero to extreme pressures with h2o and co2 as examples. International Journal of Thermophysics 16, 511–518. URL: https://doi.org/10.1007/BF01441917.

Rowe, C.D., Moore, J.C., Remitti, F., Scientists, I.E.T., 2013. The thickness of subduction plate boundary faults from the seafloor into the seismogenic zone. Geology 41, 991–994. URL: https://doi.org/10.1130/G34556.1.

Ruina, A., 1983. Slip instability and state variable friction laws. Journal of Geophysical Research: Solid Earth 88, 10359–10370. URL: https://doi.org/10.1029/JB088iB12p10359.

Rutter, E., Brodie, K., 2004. Experimental grain size-sensitive flow of hot-pressed brazilian quartz aggregates. Journal of Structural Geology 26, 2011–2023.

Scholz, C., 1998. Earthquakes and friction laws. Nature 391, 37–42. URL: https://doi.org/10.1038/34097.

Shabtian, H.S., Hirth, G., 2025. Creep of talc at subduction zone conditions: Implications for slow slip and strength of the lithosphere. Geophysical Research Letters 52, e2025GL116641. URL: https://doi.org/10.1029/2025GL116641.

Shao, T., Zhou, Y., Song, M., Ma, X., Zhang, L., Yao, W., Dang, J., Li, J., 2021. Deformation of antigorite and its geological implications. Journal of Geophysical Research: Solid Earth 126, e2021JB021650. URL: https://doi.org/10.1029/2021JB021650.

Sibson, R.H., 1982. Fault zone models, heat flow, and the depth distribution of earthquakes in the continental crust of the united states. Bulletin of the Seismological Society of America 72, 151–163. URL: https://doi.org/10.1785/BSSA0720010151.

Sly, M.K., Padilla, K., Flores, K.M., Skemer, P., 2023. Low-temperature plastic rheology of granitic feldspar and quartz. Tectonophysics 858, 229850. URL: https://doi.org/10.1016/j.tecto.2023.229850.

Sun, H., Pec, M., 2021. Nanometric flow and earthquake instability. Nature communications 12, 1–9. URL: https://doi.org/10.1038/s41467-021-26996-0.

Tse, S.T., Rice, J.R., 1986. Crustal earthquake instability in relation to the depth variation of frictional slip properties. Journal of Geophysical Research: Solid Earth 91, 9452–9472. URL: https://doi.org/10.1029/JB091iB09p09452.

Wada, I., Wang, K., 2009. Common depth of slab-mantle decoupling: Reconciling diversity and uniformity of subduction zones. Geochemistry, Geophysics, Geosystems 10. URL: https://doi.org/10.1029/2009GC002570.

Wang, K., 2024. Thermal control on the updip and downdip extents of megathrust earthquake rupture: revisiting dr. roy hyndman's seminal contributions 30 years later. Canadian Journal of Earth Sciences 62, 710–724. URL: https://doi.org/10.1139/cjes-2024-0112.

Wang, K., He, J., 2025. Downdip variations in megathrust seismogenic behavior in the japan trench subduction zone affected by mantle wedge serpentinite. Geophysical Research Letters 52, e2025GL115446. URL: https://doi.org/10.1029/2025GL115446.

Wang, K., Luo, H., He, J., Carvajal, M., 2025. Soft barrier to megathrust rupture enabled by serpentinized mantle wedge: The chile subduction zone. Earth and Planetary Science Letters 650, 119115. URL: https://doi.org/10.1016/j.epsl.2024.119115.

Wang, K., Tréhu, A.M., 2016. Invited review paper: Some outstanding issues in the study of great megathrust earthquakes—the

821 cascadia example. Journal of Geodynamics 98, 1–18. URL:
822 https://doi.org/10.1016/j.jog.2016.03.010.

Supplementary Material: Temperature Insensitive Viscous Deformation Limits Megathrust Seismogenesis

[a,b]Liam Moser, [b]Matej Pec, [b]Camilla Cattania

[a]*The MIT-WHOI Joint Program in Oceanography/Applied Ocean Science and Engineering, Cambridge and Woods Hole, MA, USA*
[b]*Department of Earth, Atmospheric and Planetary Sciences, Massachusetts Institute of Technology, Cambridge, MA, USA*

1. Frictional Failure in Terms of Differential Stress

Byerlee's rule for frictional sliding is given as

$$\tau_f = \mu\sigma_n + C, \tag{1}$$

where τ_f is the frictional shear strength, μ is the static friction coefficient, σ_n is the normal stress, and C is material cohesion. In this study, we ignore cohesion and use an effective frictional coefficient (μ') that accounts for any pore pressure induced weakening (e.g., Fisher and Hirth, 2024; Gao and Wang, 2017).

To derive a failure rule in terms of differential stress (σ_d), we assume the fault is optimally oriented. Under this condition, the failure envelope is tangent to the Mohr circle and σ_d and σ_m are related as

$$\sigma_d = 2\sin(\phi)\sigma_m, \tag{2}$$

where ϕ is the angle of internal friction (Fig. S1b). Since $\tan(\phi) = \mu'$, $\sin(\phi)$ can be re-expressed as,

$$\sin(\phi) = \frac{\tan(\phi)}{\sqrt{1+\tan^2(\phi)}} = \frac{\mu'}{\sqrt{1+(\mu')^2}}. \tag{3}$$

This gives,

$$\sigma_d = \frac{2\mu'}{\sqrt{1+(\mu')^2}}\sigma_m. \tag{4}$$

To define σ_m take the stress tensor in this model set-up to be

$$\overline{\overline{\sigma}} = \begin{bmatrix} \sigma_{txx} + \rho g z & \tau_t \\ \tau_t & \sigma_{tzz} + \rho g z \end{bmatrix}, \tag{5}$$

where τ_t is a tectonic shear stress, σ_{txx} is the horizontal tectonic stress, σ_{tyy} is the vertical tectonic stress, and $\rho g z$ is the lithostatic pressure where ρ is overburden density, g is acceleration due to gravity, and z is depth. This set up is similar to Bletery et al. (2016). The principal stresses of this tensor can be written as

$$\sigma_1,\ \sigma_3 = \rho g z + \frac{\sigma_{txx} + \sigma_{tzz}}{2} \pm \sqrt{\left(\frac{\sigma_{txx} - \sigma_{tzz}}{2}\right)^2 + \tau_t^2}. \tag{6}$$

Thus,

$$\sigma_m = \rho g z + \frac{\sigma_{txz} + \sigma_{tzz}}{2}. \tag{7}$$

Therefore, we can define $\sigma_m \approx \rho g z$ as long as the horizontal and vertical tectonic contributions are much smaller than lithostatic pressure. Remember, we account for the effect of pore pressure by modulating μ as μ', not by adjusting the ambient pressure. Combining the two assumptions, (a) that the fault is optimally oriented and (b) that mean stress is equal to lithostatic pressure, allows us to write the failure criterion as

$$\sigma_d = \frac{2\mu'}{\sqrt{1 + (\mu')^2}} \rho g z. \tag{8}$$

For plotting, we convert differential stress back to shear stress using

$$\tau = \sin\left(90 - \arctan \mu'\right) \frac{\sigma_d}{2}, \tag{9}$$

where τ is shear strength.

2. Matching Subduction Zones Between Studies

The studies Wada and Wang (2009) (thermal model WW09m), van Keken et al. (2011) (thermal model vK11m), and Heuret et al. (2011) (observed seismogenic zone depth limits) each have their own maps that define subduction zone names, locations, and dimensions. We utilized the subduction zone

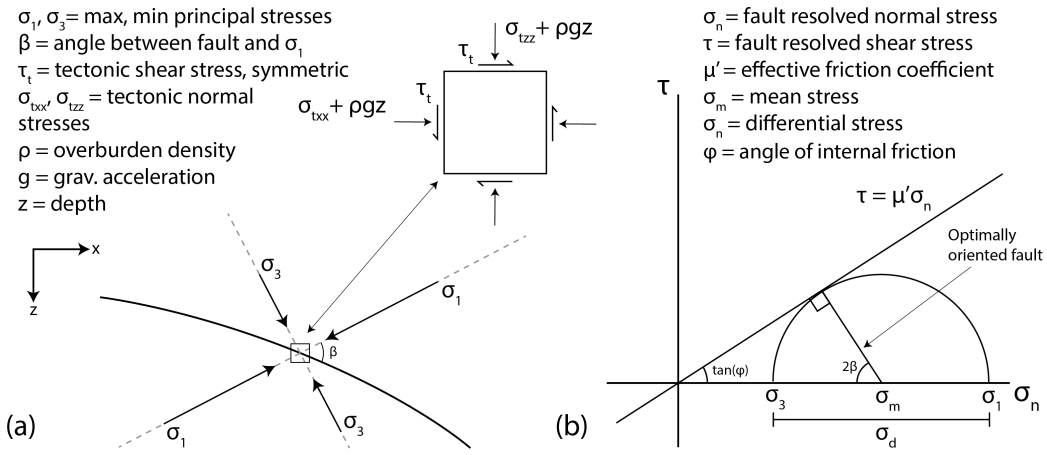

Figure 1: Diagram of frictional sliding model. (a) Fault geometry relative to principal stresses. Zoom-in shows unrotated tectonic stress tensor components. (b) Mohr circle representation of the fault stress state.

pairings for thermal models WW09m and vK11m given in van Keken et al. (2018) and, by visual inspection, selected the best matching subduction zone designation from Fig. 1 in Heuret et al. (2011). These zones were then visually matched with depth limits from Hayes et al. (2018) (Slab2) (cf., Table S3) via segment boundaries provided via personal communication (Hayes, 2023). The 17 subduction zones we use are shown in Fig. S2.

The naming conventions for each subduction zone in the thermal model WW09m, thermal model vk11m, and seismogenic zone depth limit observations are given in Table S1. These names can be used to recover the original data from the supporting information of each source.

3. Thermals Models and Shear Heating

As discussed in *Section 2: Data Overview* we use thermal models with shear heating due to $\mu'_{sh} = 0.03$ and 0.12. Shear heating occurs during rapid slip, and thus this coefficient is the dynamic friction coefficient and is separate from the interseismic effective friction coefficient (μ'), which we use in this paper to determine peak static fault strength. A coefficient of $\mu'_{sh} = 0.03$ is the representative value used by van Keken et al. (2018) that produces heat fluxes consistent with observations in the Japan and Cascadia subduction zones (cf., $f_{arbi} = 1$ for vK11m in van Keken et al. (2018)). However, rougher and geometrically complex megathrusts, such as Hikurangi, can have a factor

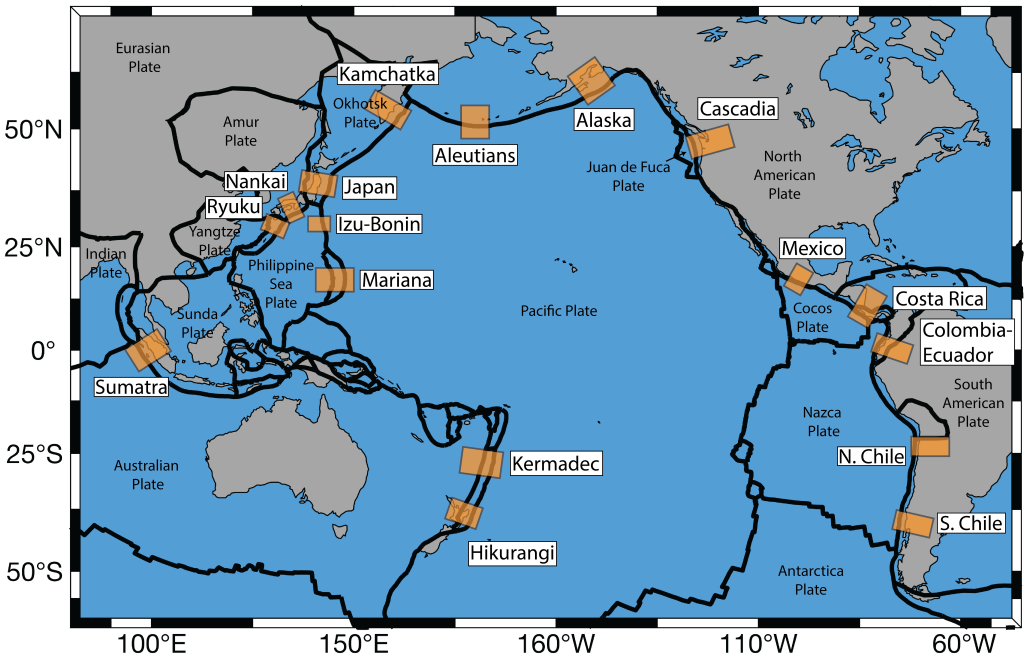

Figure 2: Reference map of the 17 subduction zones used in this study and their naming conventions. Map is a modified version of the map in Wada and Wang (2009). Orange boxes denoting subduction zones were placed by visual inspection to match Wada and Wang (2009).

of 5 greater μ'_{sh} (Gao and Wang, 2014). We assess this variation by taking $\mu'_{sh} = 0.12$ across all subduction zones, equivalent to $f_{arbi} = 4$ for vK11m (Table S2).

Increasing μ'_{sh} increases the temperature along the slab while decreasing μ'_{sh} has the opposite effect. The depth limits for thermal models vK11m and WW09m with shear heating at $\mu'_{sh} = 0.03$ are, on average, 62 and 66°C warmer, respectively, than without shear heating. While the average increase is the same for both models, the effect of shear heating is more uniform for vK11m than WW09m, with a standard deviation of 12 versus 43°C. Regardless, both standard deviations are an order of magnitude smaller than the full temperature range spanned by the observed depth limits (vK11m=210-470°C, WW09m=125-490°C) and thus removing shear heating level will not remove the temperature independence (i.e., the wide range of temperatures) at the observed depth limits.

In the main text we utilize thermal model vK11m instead of WW09m

Table 1: Subduction zone naming conventions and segment matches between studies. Names are from the Supporting Information of van Keken et al. (2018), Table 1 of Heuret et al. (2011), and Table S3 from Hayes et al. (2018).

This study	WW09m	vK11m	Heuret et al. (2011)	Slab2
Cascadia	1-Cascadia8Ma_SedTem	04_Cascadia	Cascades	Cascadia
Nankai	2-Nankai_SedTem	46_Nankai	Nankai	Nankai
Mexico	3-MexicoN	05_Mexico	Mexico	Mexico
Costa Rica	10-CostaRica	08_Costa_Rica	Cocos	El Salvador
Colombia-Ecuador	4-Colombia_SedTem	09_Colombia_Ecuador	Colombia	Colombia
Aleutians	11-Aleutians_SedTem	54_C_Aleut	C-Aleutians	Central Aleutians
S. Chile	5-SChile_SedTem	18_S_Chile	S-Chile	Southern Chile
Hikurangi	12-Hikurangi	37_New_Zealand	Hikurangi	New Zealand
Ryuku	6-Kyushu_SedTem	44_Kyushu	N-Ryukyu	Central Ryukyu
Mariana	13-Mariana	40_S_Marianas	Marianas	North Mariana
Sumatra	7-Sumatra_SedTem	24_C_Sumatra	Sumatra	Sumatra
Kermadec	14-Kermadec	36_Kermadec	N-Kermadec	Central Kermadec
Alaska	8-Alaska_SedTem	02_Alaska	E-Alaska	Alaska
Kamchatka	15-Kamchatka	52_Kamchatka	Kamchatka	Kamchatka
N. Chile	9-NChile	14_NC_Chile	N-Chile	Northern Chile
Izu-Bonin	16-Izu	43_Izu	Izu-Bonin	Izu
Japan	17-NEJapanC	48_N_Honshu	Japan	Japan

since it includes flat-slab subduction in Mexico and produces lower misfits during the grid-search inversion (Table 2). Regardless of model choice, the root-mean-square difference in minimum misfit between the two thermal models across all creep mechanisms is only 3.3 km and thus the choice of model does not affect our conclusions. The lower misfits for the vK11m grid-search inversions are likely due to vK11m's observed depth limit temperatures spanning a smaller range than WW09m (Fig. 2c, d). Since observed depth limits are relatively constant ($\sim$50 km) a smaller temperature range slightly reduces the need for creep mechanisms to be temperature insensitive. This improves fit as all creep mechanisms are at least somewhat temperature dependent.

The updip extent of the thermal models ranges from 3.6 to 16 km, and the downdip between 130 km and 407 km, encompassing all observed depth limits. To avoid numerical issues when exploring FVT model parameters, we interpolate to 0°C at 0 km and 1566°C at 410 km depth (Katsura, 2022); however, no well-fitting model should rely on these interpolated values. For each subduction zone, overriding plate Moho depth comes from Wada and Wang (2009).

4. Unconstrained Power Law Grid-Search Inversion

We invert for the best fitting power law FVT in two ways, which we refer to as lab-constrained and unconstrained. The main text focuses on the lab-

Table 2: Summary of FVT results by viscous creep mechanism for shear heating level $\mu'_{sh} = 0.12$ compared to $\mu'_{sh} = 0.03$. All Heuret et al. (2011) depth limits and thermal model vK11m are used.

Creep mechanism	**Min. misfit (km)** $\mu'_{sh} = 0.03/0.12$	**Within bounds**	**Residual slope**	**Residual** R^2
Quartz dislocation	11.3/12.2	yes/yes	0.62/0.71	0.72/0.61
Quartz diffusion	33.0/25.8	no/no	N/A	N/A
Albite dislocation	21.1/15.6	no/yes	-/0.78	-/0.78
Albite diffusion	17.7/16.2	no/yes	-/0.79	-/0.80
Wet olivine dislocation	30.0/20.7	no/no	N/A	N/A
Wet olivine diffusion	31.1/22.6	no/no	N/A	N/A
Quartz LTP	26.9/17.1	no/no	N/A	N/A
Plagioclase LTP	19.0/8.8	no/no	N/A	N/A
Dry olivine LTP	13.3/7.5	no/yes	-/0.40	-/0.17
Wet olivine LTP	5.6/6.7	yes/yes	-0.13/0.09	0.02/0.00
Antigorite LTP	6.5/9.3	yes/yes	0.35/0.56	0.25/0.38
Talc LTP	5.6/6.8	yes/yes	0.00/-0.02	0.00/0.00

constrained method; however, both methods are fundamentally similar and grid-search based. Here we discuss the unconstrained approach.

The unconstrained method is not tied to a single lab-constrained parameter set. Instead, we define plausible ranges for all parameters that make up the lumped parameters C_1 and C_2 (Table S3, Eq. 8). We then calculate the maximum and minimum values of each C_1 and C_2 from the predefined ranges of their constituent parameters, with these values forming the upper and lower bounds for the grid search. The initial grid search is for a 300 by 301 grid of C_1 and C_2. We identify a minimum misfit location on this grid, reduce the bounds, and repeat the grid search at a lower resolution. This process is carried out three times to identify the best-fitting C_1 and C_2 pair.

Figs. S5, S6 show the results of the unconstrained inversion for thermal model vK11m and WW09m, respectively. For reference, the location of the experimental results for quartz dislocation creep, albite dislocation creep, and albite diffusion creep (Table 1), spanning $\mu' = 0.03 - 0.6$ and $\dot{\epsilon} = 5.2 \times 10^{-13} - 3.7 \times 10^{-10}$ 1/s are overlain on the grid search misfit space. We unpack the constituent FVT parameters for both the minimum misfit C_1 and C_2 as well as the C_1 and C_2 ranges consistent with a 10 km misfit level.

Table 3: Power law parameter ranges used to bound the unconstrained grid-search based inversion. We use a larger strain rate range that encompasses the smaller, more physical, range used for the forward models.

Power law	Symbol	Value	Units
Stress exponent	n	1 - 4	unitless
Grain size	d	15	μm
Grain size exponent	m	3	unitless
Water fugacity	f_{H_2O}	250 - 550	MPa
Water fugacity exponent	r	1	unitless
Pre-factor	A	10^{-20} - 10^{10}	$\mu\mathrm{m}^{\mathrm{m}}/(\mathrm{s}\cdot\mathrm{MPa}^{\mathrm{n+r}})$
Activation energy	Q	2 - 600	kJ/mol
Strain rate	$\dot{\epsilon}$	10^{-20} - 10^{-10}	1/s
Ideal gas constant	R	8.314472	kJ/(mol·°K)
Frictional			
Effective friction coefficient	μ'	0.01 - 0.7	unitless
Overburden density	ρ	2,900	kg/m^3
Accel. due to gravity	g	9.8	m/s^2
Lumped			
Power law 1	$\log_{10}(C_1)$	-27.73 - 14.38	km
Power law 2	C_2	60.14 - $72,163$	°K

5. Further Discussion of Heuret et al. (2011) versus Slab2

Heuret et al. (2011) and Hayes et al. (2018) (Slab2) are our depth limit observation sources. The main text analysis focuses on Heuret et al. (2011) and we use Slab2 to reinforce our conclusions. As discussed in the main text, Heuret et al. (2011) events are from the Harvard Centroid Moment Tensor catalog (Dziewonski et al., 1981) with hypocenter locations dictated by the EHB bulletin (Engdahl et al., 1998), with events from 1976-2007 used. For an event to be used to define the seismogenic zone in Heuret et al. (2011), it must have a nodal plane pointing at the volcanic arc, a strike of $\pm 45°$ to the trench, and a dip $\pm 20°$ from known slab geometry.

There are three main processing differences between Heuret et al. (2011) and Slab2. First, Slab2 is more recent and uses the Advanced National Seismic System Combined Catalog (ComCat) (USGS, 2018) to source megathrust events. However, ComCat includes the EHB catalog used by Heuret et al. (2011) and thus both papers rely, in part, on the same data. Second, Slab2 defines the depth limit as the 90$^{\mathrm{th}}$ percentile of the earthquake depth

distribution, while Heuret et al. (2011) takes the 95$^{\text{th}}$ percentile. The Heuret et al. (2011) depth limits are, on average, 5.2 km deeper than Slab2, and this depth difference is likely, at least in part, due to the percentile change. Third, the papers define and treat subduction zones with poorly constrained depth limits differently. Both papers use the number of earthquakes to define whether a subduction zone is poorly constrained. The threshold is N<10 and N<50 earthquakes for Heuret et al. (2011) and Slab2, respectively. The poorly constrained subduction zones are: Cascadia, Nankai, Southern Chile, and Alaska for Heuret et al. (2011), and Nankai, Cascadia, and Hikurangi for Slab2. The poorly constrained subduction zones, setting aside Alaska which is well constrained by Slab2, are unique as they consist of young and warm oceanic lithosphere (Cascadia, Nankai, and Southern Chile) or are a special case such as the subduction of the Hikurangi Plateau off New Zealand (Bassett et al., 2025). To address this poor constraint, Slab2 fully omits these subduction zones from their analysis of seismogenic zone width. On the other hand, Heuret et al. (2011) replaces these poorly constrained subduction zones with depth limits from Oleskevich et al. (1999). However, the Oleskevich et al. (1999) depth limits rely on both geodetic modeling and great earthquake co-seismic slip and fall outside the scope of how we define the megathrust seismogenic zone. Here we consider the effect of Heuret et al. (2011) versus Slab2 and all subduction zones versus well-constrained subduction zones with four test cases: (1) all subduction zones from Heuret et al. (2011), (2) all subduction zones from Slab2, (3) only well-constrained Heuret et al. (2011) subduction zones, (4) only well-constrained Slab2 subduction zones (Table S4). This allows us to keep as consistent a definition of the seismogenic zone as possible (i.e., defined by small to medium interplate earthquake hypocenters).

The best fitting FVT mechanisms do not depend on which case is used (Table S4). Across all cases, quartz dislocation creep remains both the best fitting power law creep mechanism (mean minimum misfit = 11 ± 1.5 km) and the only power law creep mechanism to fit the observed limits within the geologically plausible effective friction coefficient and strain rate ranges. This across case consistency holds for LTP, where wet olivine, antigorite, and talc remain the best fitting mechanisms (mean minimum misfit = $5.8 \pm 1.1\sigma$ km) and the only LTP mechanisms to fit observed limits within the geologically plausible parameter ranges. The fact that quartz dislocation creep is too temperature-sensitive to reach the ∼6 km LTP misfit level also holds. In each case, quartz dislocation has a predicted-depth versus model-residual

slope that is positive with $R^2 > 0.7$, with both values larger than each case's respective LTP mechanisms. While the residual slopes for the case with all-Slab2-subduction-zones are positive and much larger (>0.5) than for the all-Heuret et al. (2011) case, the LTP R^2 remains low in comparison to quartz dislocation creep. This low R^2 shows that the residuals aren't well explained by the line of best fit and thus LTP is not under-predicting the depth of warm subduction zones and over-predicting the depth of cold subduction zones as much as quartz dislocation creep is. This difference can be seen visually in Fig. S7.

6. Uncertainty in Observed Depth Limits and Comparison to Local Studies

As discussed in the main text, subduction zone seismogenic depth limits inherently depend on how the seismogenic zone is defined and here we focus on earthquake nucleation and the hypocentral depth of extent of small to medium earthquakes (Wang and Tréhu, 2016). However, the earthquake depth distribution depends on the temporal-length and spatial-scale over which the observations are made. Longer station deployments increase the number of events overall and thus the likelihood of deeper events that increase the observed depth limit. Denser station spacing increases the catalog magnitude completeness to the same effect. Heuret et al. (2011) quantified this uncertainty by comparing their depth limits from a global teleseismic catalog to local studies. They found that they underestimated subduction zone seismogenic zone width by 10% when N>100 earthquakes and by 30-50% when N<20 earthquakes. However, this comparison was made against great earthquake rupture extent and thermally defined seismogenic zones in addition to local earthquake catalogs and thus partially violates our definition of the seismogenic zone. Regardless, using the dip angles from Heuret et al. (2011) we plot this correction in Fig. S8 and show that it does not improve rate-and-state or Moho control model fit or alter the large variation in temperature ($> 250°$C) across all 17 subduction zones.

For a portion of the subduction zones we carried out a comparison of the Heuret et al. (2011) and Slab2 depth limits with local studies and, opposite to Heuret et al. (2011), did not find evidence that observed depth limits were systematically underestimated. In fact, in all cases the observed depth limits from Heuret et al. (2011) and Slab2 matched the local studies well or were an overestimate. Overestimation is especially common for poorly

constrained subduction zones. However, we have shown that their inclusion is not fundamental to this study's conclusions. We detail our local comparison in the following list.

- The **Cascadia Subduction Zone** is poorly constrained by both Heuret et al. (2011) and Slab2, with a depth limit of 30 and 42 km, respectively. Heuret et al. (2011) actually reports zero earthquakes and takes the limit from Oleskevich et al. (1999), who uses geodetic data. Slab2 uses 21 events. A local catalog built by template matching reports a depth limit of 20-25 km (Morton et al., 2023) and geodetically-inferred plate locking gives ∼19 km for Northern Cascadia (Sherrill et al., 2024).

- The **Nankai Subduction Zone** is poorly constrained by both Heuret et al. (2011) and Slab2, with a depth limit of 35 and 51 km with N=5 and N=28 events, respectively. Heuret et al. (2011) takes the limit from Oleskevich et al. (1999), who use geodetic data. Local studies report a ∼25 km depth limit using geodetically-inferred plate locking (Sherrill et al., 2024) and great earthquake rupture extent (Bassett et al., 2022).

- The **Hikurangi Subduction Zone** is poorly constrained in Slab2 with a depth limit of 38 km and N=34 earthquakes. However, Heuret et al. (2011) marks it as well-constrained with a depth limit of 61 km, even though N=8 events. Local studies of geodetically-inferred plate locking (Bassett et al., 2025; Wallace et al., 2012) and large interface events (Wallace et al., 2009) report a depth ∼35-40 km, consistent with Slab2.

- The **Southern Chile Subduction Zone** is well constrained by Slab2 with a depth limit of 38 km and N=352 earthquakes, but poorly constrained by Heuret et al. (2011) with a depth limit of 50 and N=8. Heuret et al. (2011) takes the depth limit from Oleskevich et al. (1999), who use the 1960 great earthquake and its aftershocks to constrain the depth limit. The more recent local study of Lange et al. (2007) report a depth limit of ∼30 km, using a catalog developed with ocean-bottom seismometer data, though their data cannot define a clear limit.

- The **Japan Trench** is well constrained by both Heuret et al. (2011) and Slab2, with depth limits of 60 and 51 km with N=205 and N=721 events, respectively. The local earthquake studies of Igarashi et al. (2001, 2003) report a depth of ∼50 km when calculated along the Slab2

slab model (Hayes et al., 2018)(c.f., Fig. 5, Igarashi et al., 2003). The local studies of Kawakatsu and Seno (1983); Seno (2005) report a depth of 60-70 km, due the "cloud" of thrust-type events defining a deeper and wider range without the use of a slab model.

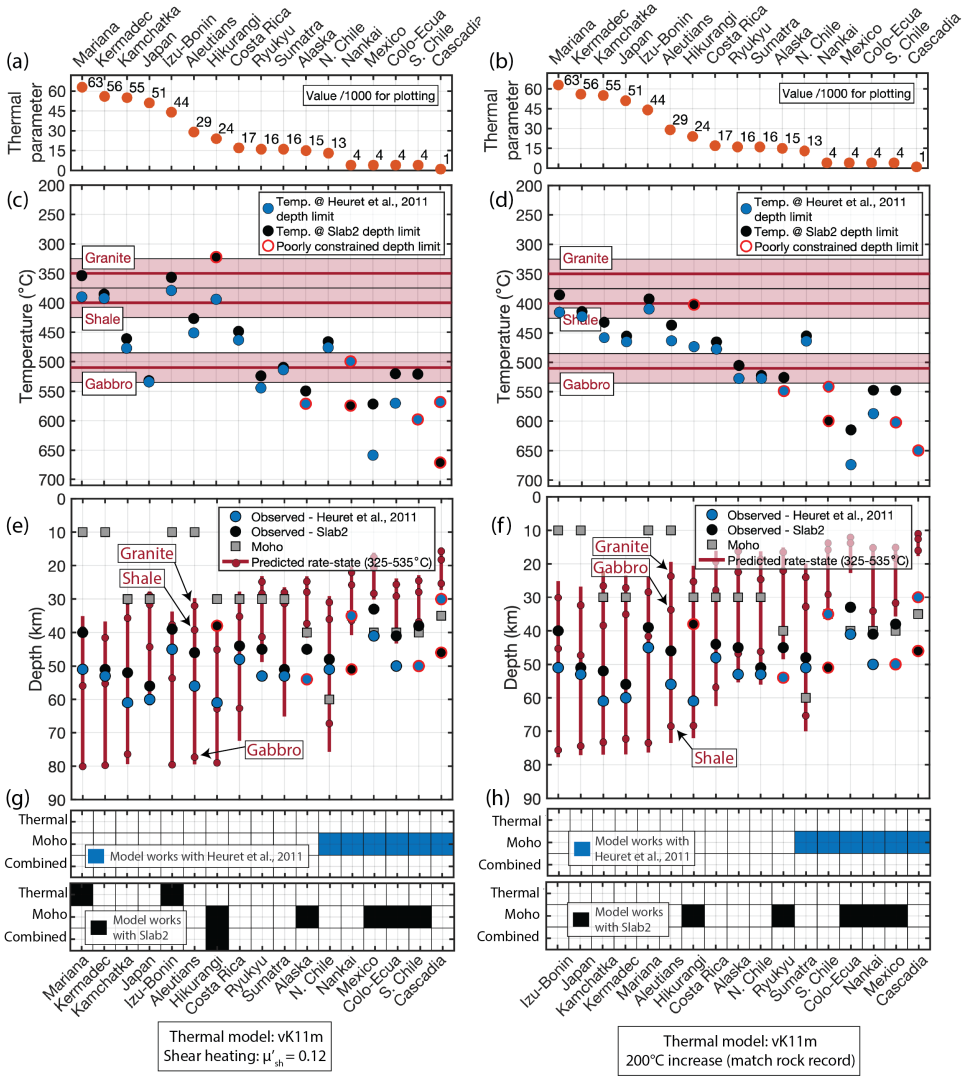

Figure 3: Same as Fig. 2 but adjusted to show effect of increasing shear heating via $\mu'_{sh} = 0.12$ (left column) or a 200°C uniform increase to match petrologically-inferred geotherm temperatures (right column). Thermal model vK11m is used.

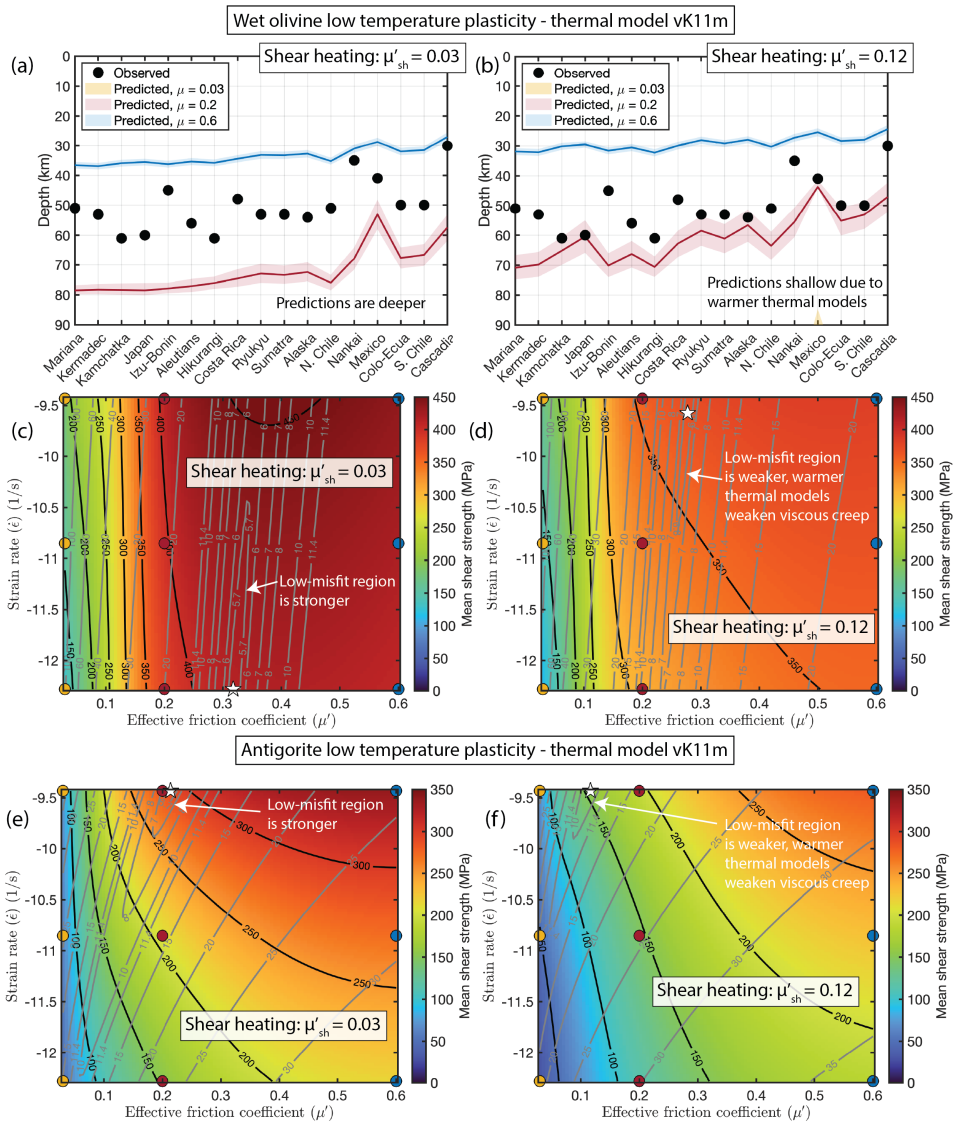

Figure 4: Increasing thermal model shear heating shallows FVT depth predictions and reduces the strength of the best fitting models. (a) Lab-constrained forward models of wet olivine LTP for shear heating with $\mu'_{sh} = 0.03$. (b) Same as (a) except for $\mu'_{sh} = 0.12$. (c)(d) Full grid search root-mean-square and misfit space for wet olivine LTP with (c) $\mu'_{sh} = 0.03$ and (d) $\mu'_{sh} = 0.12$. (e)(f) Same as (c)(d) but for antigorite LTP.

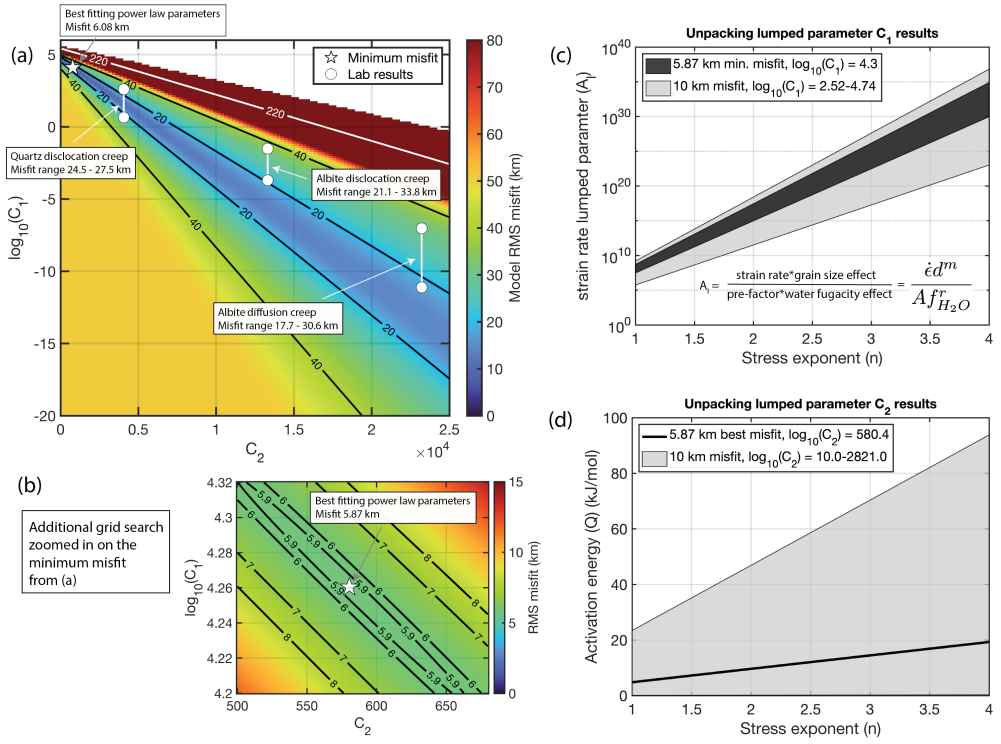

Figure 5: Grid search for best fitting power law FVT parameters using thermal model vK11m (RMS = root-mean-square). (a) Largest scale grid search covering a wide FVT parameter range (Table S3). White circles with connecting lines denote power law creep lab results for a C_1 range encompassed by $\mu' = 0.03 - 0.6$ and $\dot{\epsilon} = 5.2 \times 10^{-13} - 3.7 \times 10^{-10}$ 1/s. (b) Localized grid search around minimum misfit in (a). (c) Allowed FVT parameters for the best fitting parameter C_1 and the range of C_1 with a 10 km misfit. (d) Same as (c) but for parameter C_2.

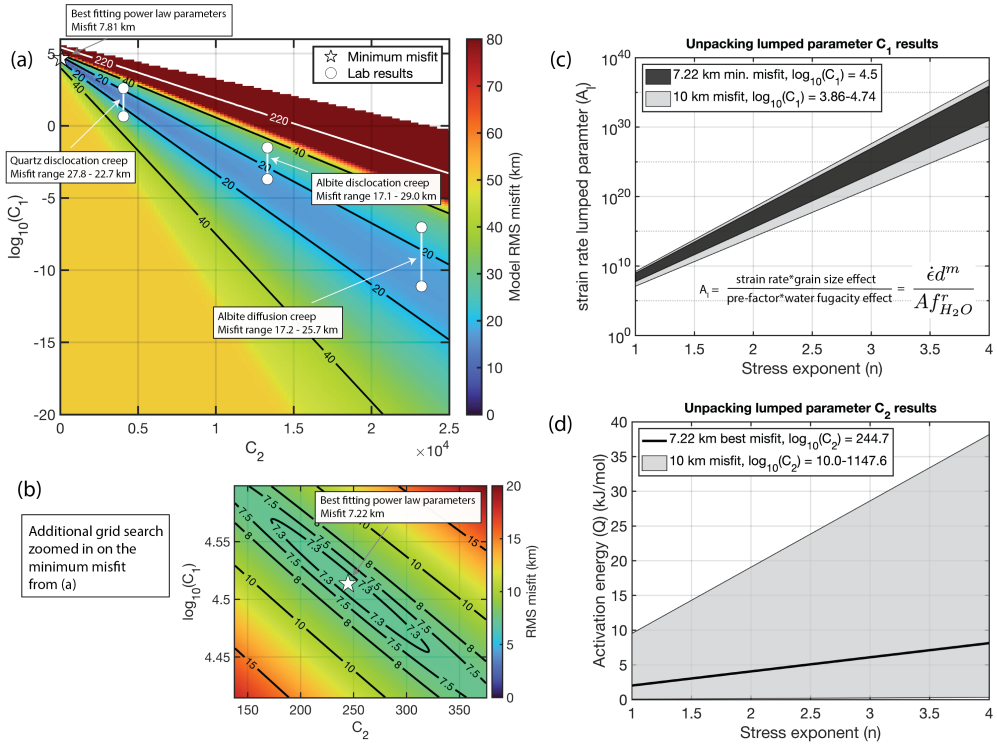

Figure 6: Same as Fig. S5 but for thermal model WW09m.

Table 4: Table summarizing FVT model results for Heuret et al. (2011) versus Slab2 depth limit observations both for all subduction zones and only well-constrained subduction zones. For each FVT model case results are given as [all-Heuret]/[all-Slab2]/[well-constrained-Heuret]/[well-constrained-Slab2]. Thermal model vK11m is used for this analysis.

Creep mechanism	**Min. misfit (km)**	**Within bounds**
Quartz dislocation	11.3/13.8/10.8/10.7	yes/yes/yes/yes
Quartz diffusion	33.0/38.1/31.4/38.6	no/no/no/no
Albite dislocation	21.1/27.6/22.9/28.0	no/no/no/no
Albite diffusion	17.7/24.2/19.8/23.8	no/no/no/no
Wet olivine dislocation	30.0/35.3/28.8/36.0	no/no/no/no
Wet olivine diffusion	31.1/36.3/29.7/36.9	no/no/no/no
Quartz LTP	26.9/32.2/26.0/32.9	no/no/no/no
Plagioclase LTP	19.0/24.4/18.6/24.9	no/no/no/no
Dry olivine LTP	13.3/19.1/13.8/19.4	no/no/no/no
Wet olivine LTP	5.6/5.1/4.7/5.0	yes/yes/yes/yes
Antigorite LTP	6.5/8.7/6.4/6.1	yes/yes/yes/yes
Talc LTP	5.6/5.8/4.7/5.0	yes/yes/yes/yes
Creep mechanism	**Residual slope**	**Residual R^2**
Quartz dislocation	0.62/0.90/0.76/0.75	0.72/0.81/0.79/0.74
Quartz diffusion	N/A	N/A
Albite dislocation	N/A	N/A
Albite diffusion	N/A	N/A
Wet olivine dislocation	N/A	N/A
Wet olivine diffusion	N/A	N/A
Quartz LTP	N/A	N/A
Plagioclase LTP	N/A	N/A
Dry olivine LTP	N/A	N/A
Wet olivine LTP	-0.13/0.56/0.11/-0.04	0.02/0.12/0.01/0.00
Antigorite LTP	0.35/0.80/0.57/0.50	0.25/0.55/0.44/0.30
Talc LTP	0.00/0.39/-0.12/-0.05	0.00/0.03/0.01/0.00

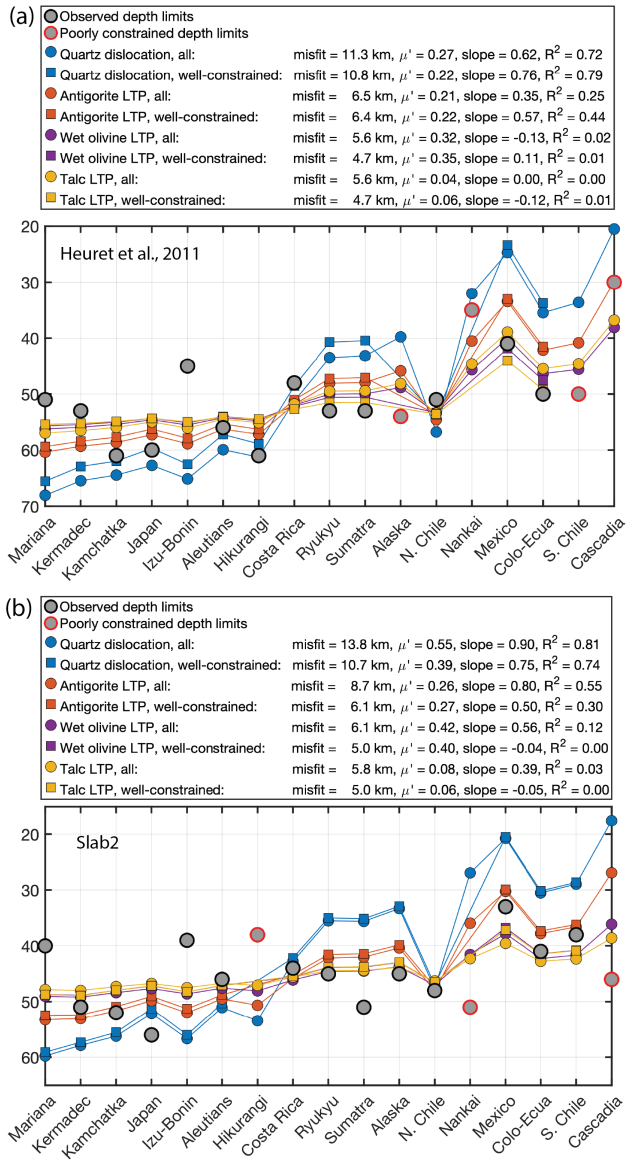

Figure 7: Comparison of FVT model results from the grid-search inversion. (a) Inversions with depth limit observations from Heuret et al. (2011). Gray circles are observed depth limits. Red outlines mark poorly constrained subduction zones that are excluded for the well constrained inversion. Final inversion values in legend match those in Table S4. (b) Same as (a) except for Slab2.

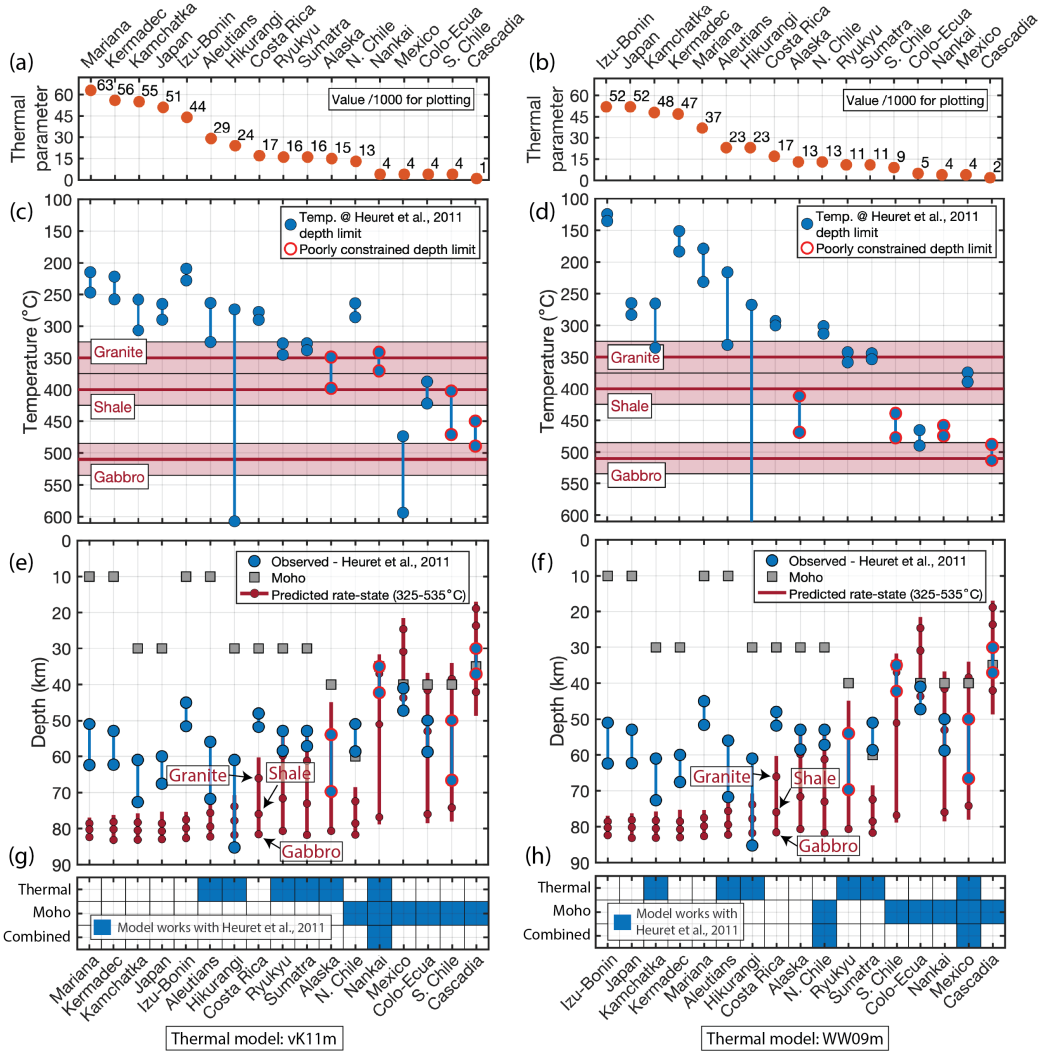

Figure 8: Adaptation of Fig. 2 to include estimate of how much Heuret et al. (2011) underestimates the observed depth limit in comparison to local studies. Underestimates are given as percentage changes in the Supplementary Material of Heuret et al. (2011). Each colder/hotter and shallower/deeper pair of blue circles represents the original depth limit and the updated "local study" depth limit. For evaluating the Moho control model (g)(h), we consider if the range between these estimates overlaps 350 ± 25°C or the Moho. Slab2 is not plotted. Everything else remains identical to Fig. 2.

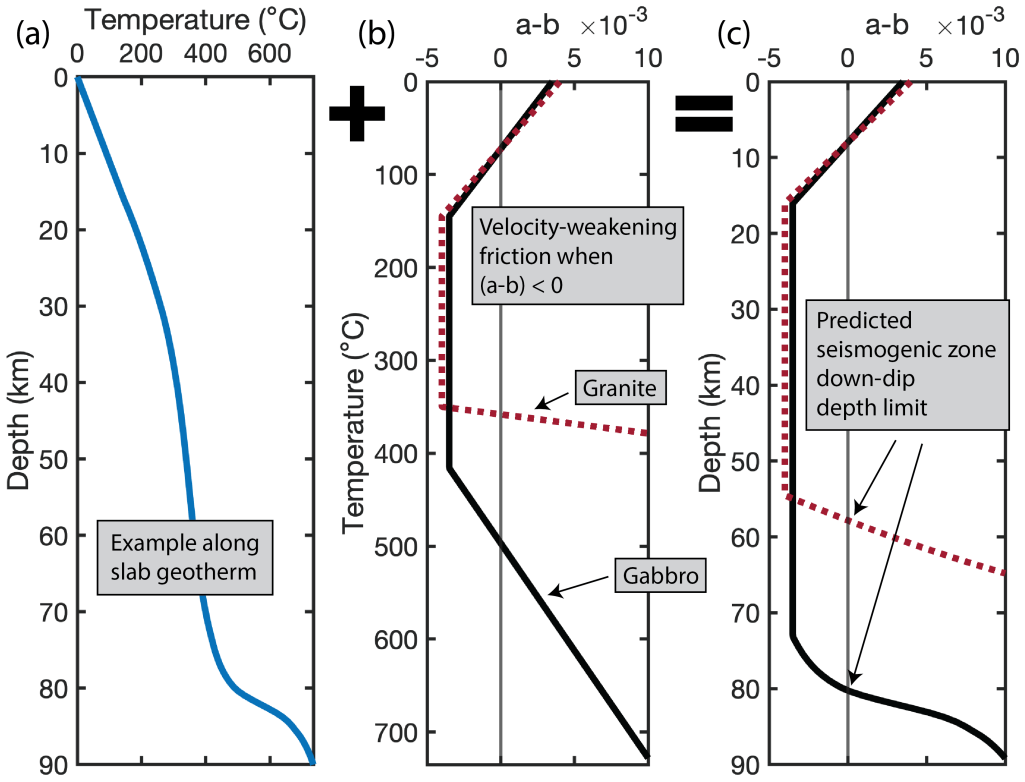

Figure 9: (a) Example along slab geotherm for Alaska (thermal model vK11m). (b) Temperature dependence of rate-and-state $a-b$ parameter for different experiments. Red dashed line is granite gouge from Blanpied et al. (1998) and black line is gabbro gouge from He et al. (2007). (c) Resulting along slab $a-b$ profile from combining experimental temperature dependence with the along slab geotherm model. The downdip location where $a-b>0$ marks the predicted bottom of the seismogenic zone.

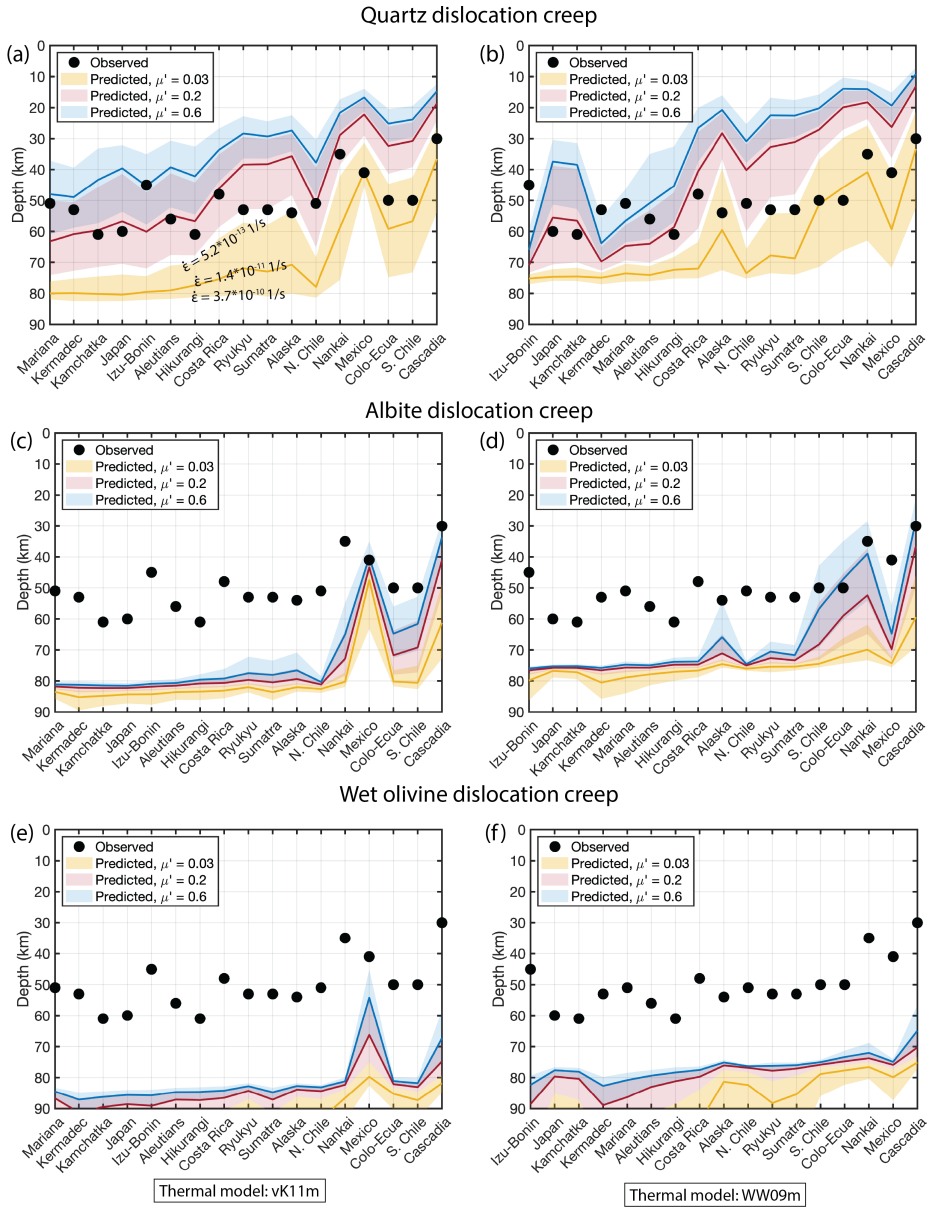

Figure 10: Frictional-viscous transition predictions for power law dislocation creep. Each row is a different mineral with thermal models separated by column. Black circles are the observed seismogenic zone depth limits. Color denotes effective friction coefficient. Each colored patch is the range of predictions between the minimum and maximum strain rate of 5.2×10^{-13} and 3.7×10^{-10} 1/s and the solid lines denote the mean strain rate of 1.4×10^{-11} 1/s

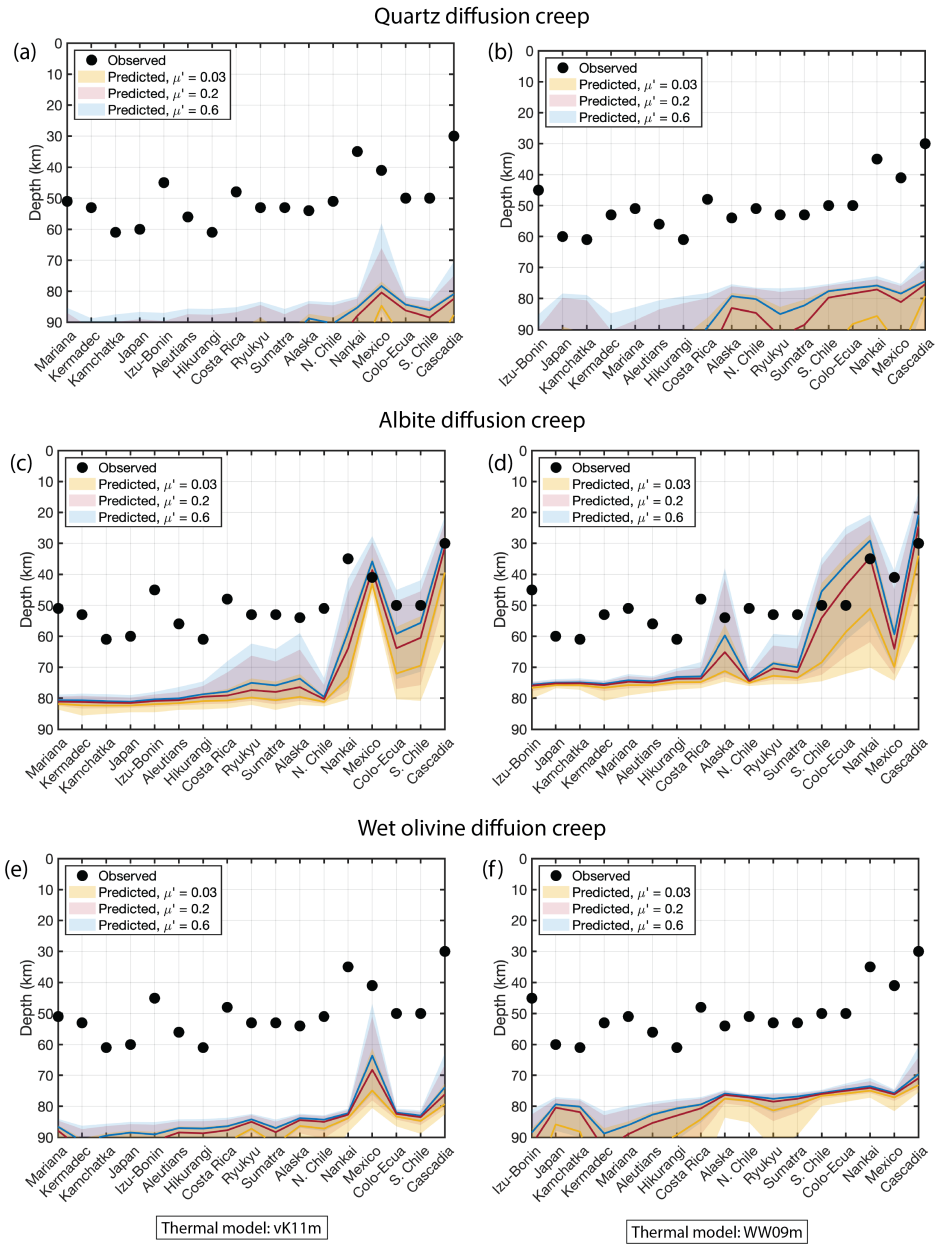

Figure 11: Same as Fig. 10 but for diffusion creep.

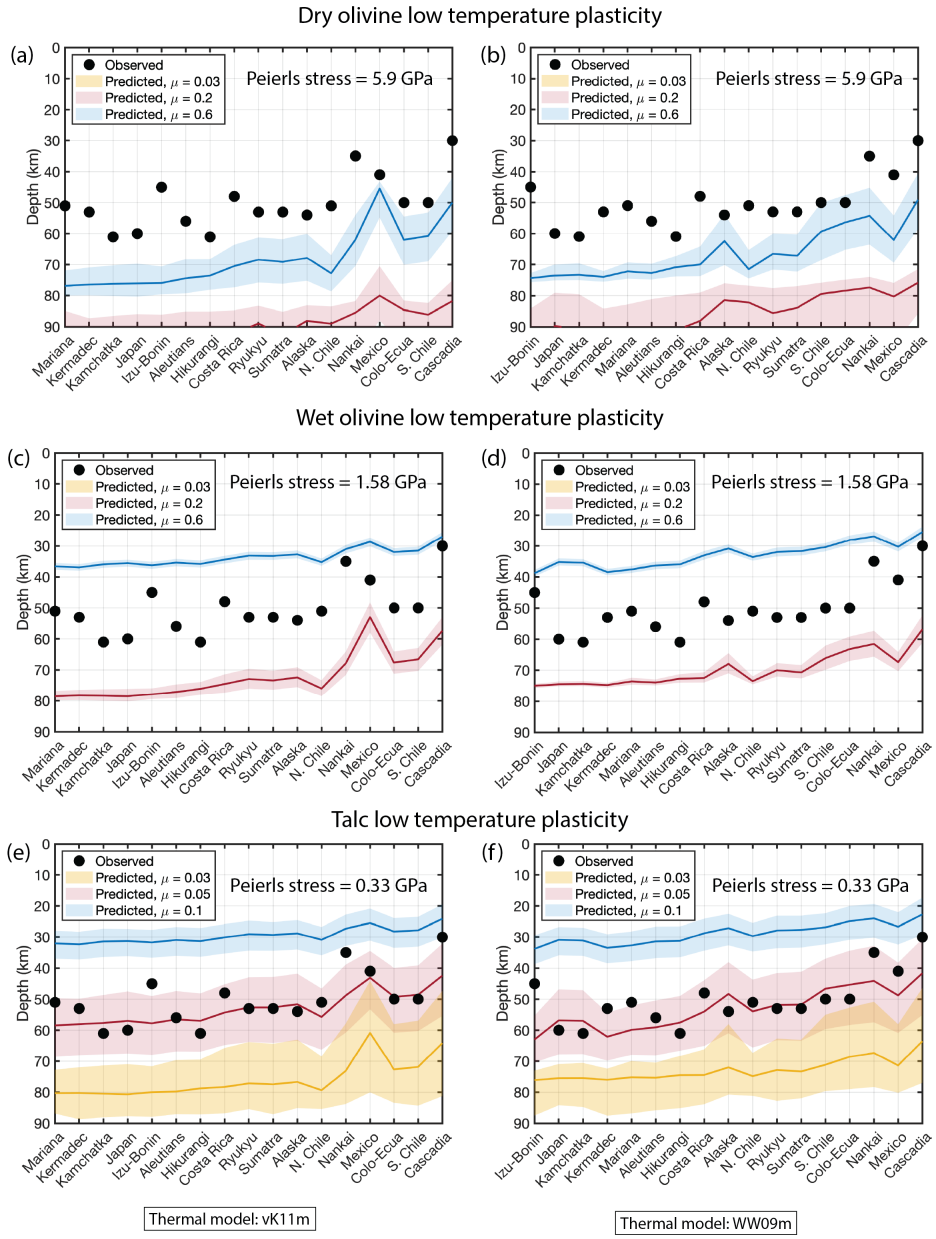

Figure 12: Frictional-viscous transition predictions for LTP. Each row is a different mineral with thermal models separated by column. Black circles are the observed seismogenic zone depth limits. Color denotes effective friction coefficient. Each colored patch is the range of predictions between the minimum and maximum strain rate of 5.2×10^{-13} and 3.7×10^{-10} 1/s and the solid lines denote the mean strain rate of 1.4×10^{-11} 1/s

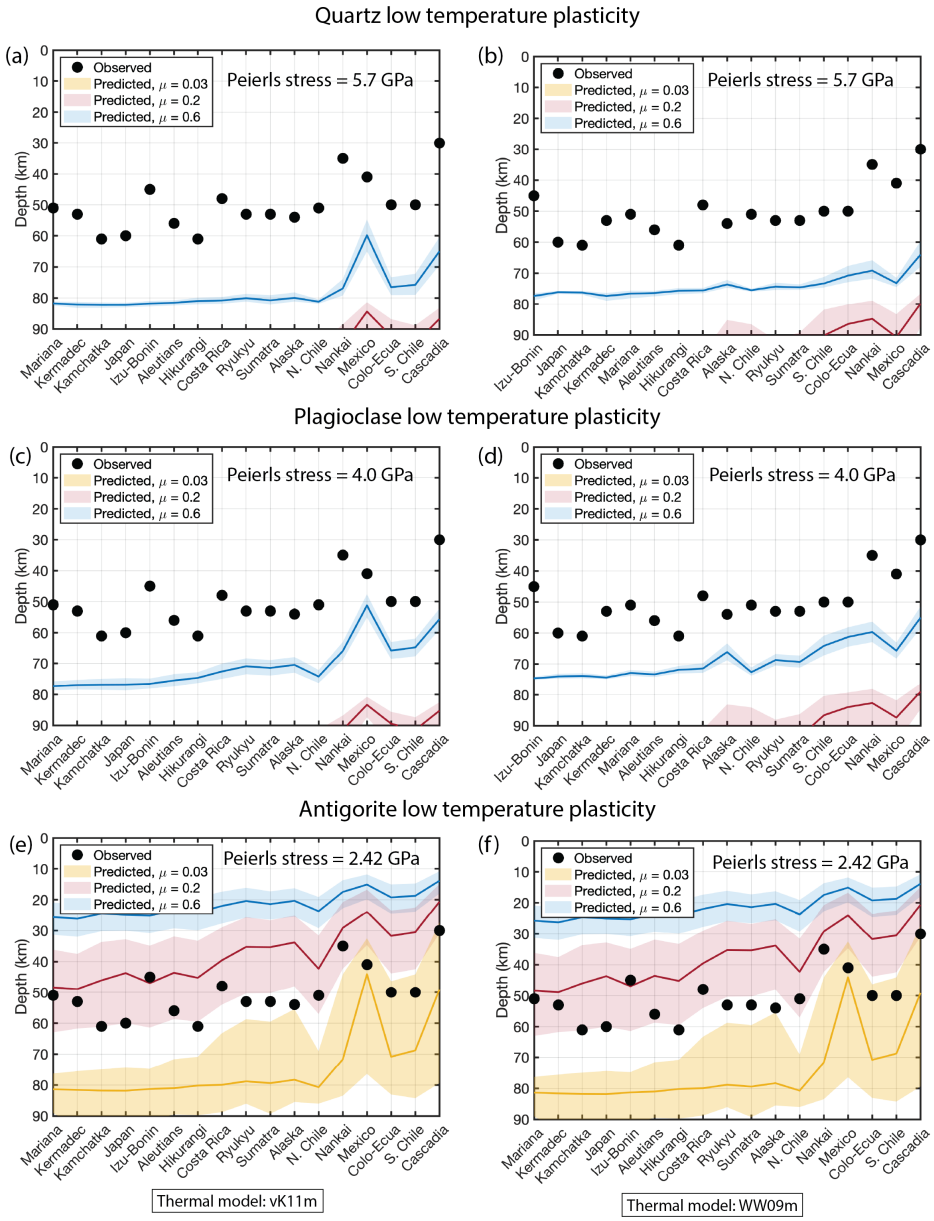

Figure 13: LTP frictional-viscous transition predictions for more minerals. Everything else is identical to Fig. S12.

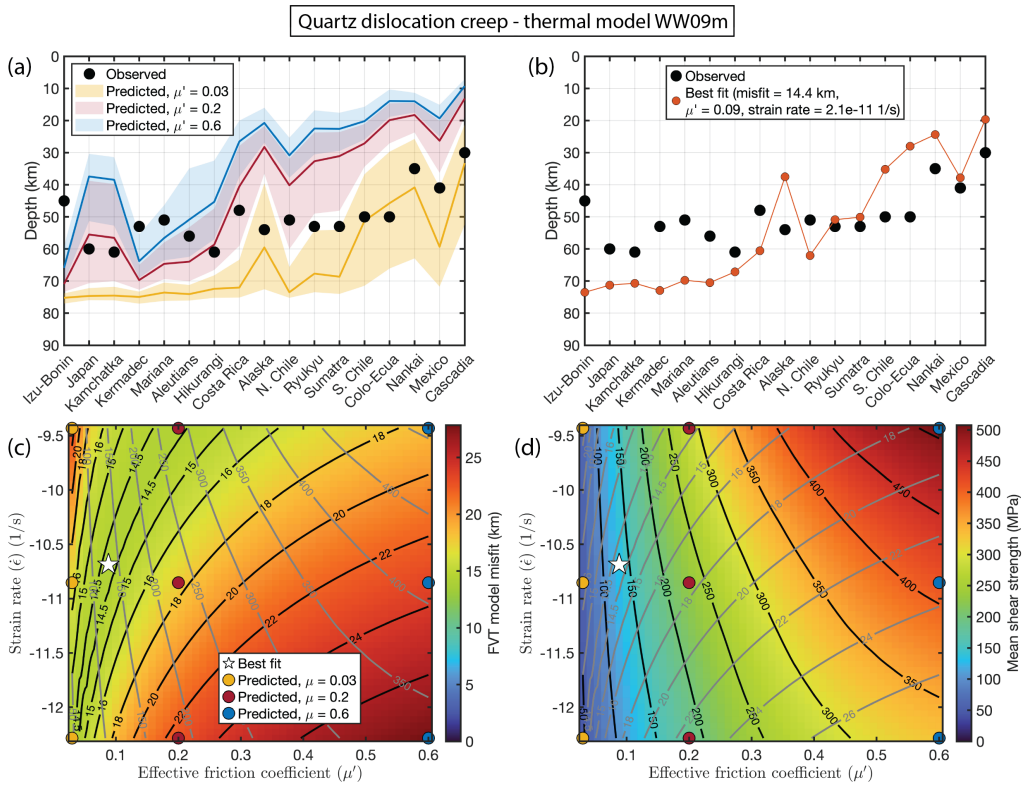

Figure 14: FVT inversion for quartz dislocation creep with thermal model WW09m. (a) Lab constrained forward models. (b) Best fitting model between $\mu' = 0.03 - 0.6$ and $\dot{\epsilon} = 5.2 \times 10^{-13} - 3.7 \times 10^{-10}$ 1/s. (c) Grid search with black lines as root-mean-square misfit contours. Gray contours are mean shear strength. White star denotes best fitting model shown in (b) and circles are parameters of forward models plotted in (a). (d) Same as (c) except for mean shear strength of all 17 subduction zones at the predicted FVT.

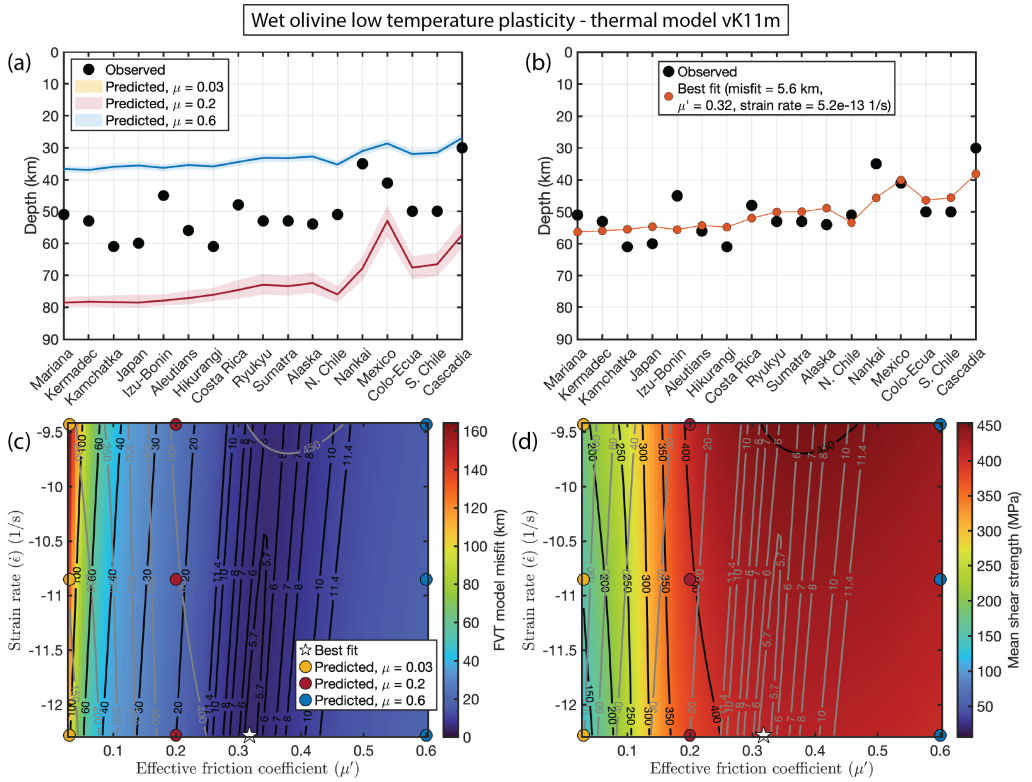

Figure 15: FVT inversion for wet olivine LTP with thermal model vK11m. (a) Lab constrained forward models. (b) Best fitting model between $\mu' = 0.03 - 0.6$ and $\dot{\epsilon} = 5.2 \times 10^{-13} - 3.7 \times 10^{-10}$ 1/s. (c) Grid search with black lines as root-mean-square misfit contours. Gray contours are mean shear strength. White star denotes best fitting model shown in (b) and circles are parameters of forward models plotted in (a). (d) Same as (c) except for mean shear strength of all 17 subduction zones at the predicted FVT.

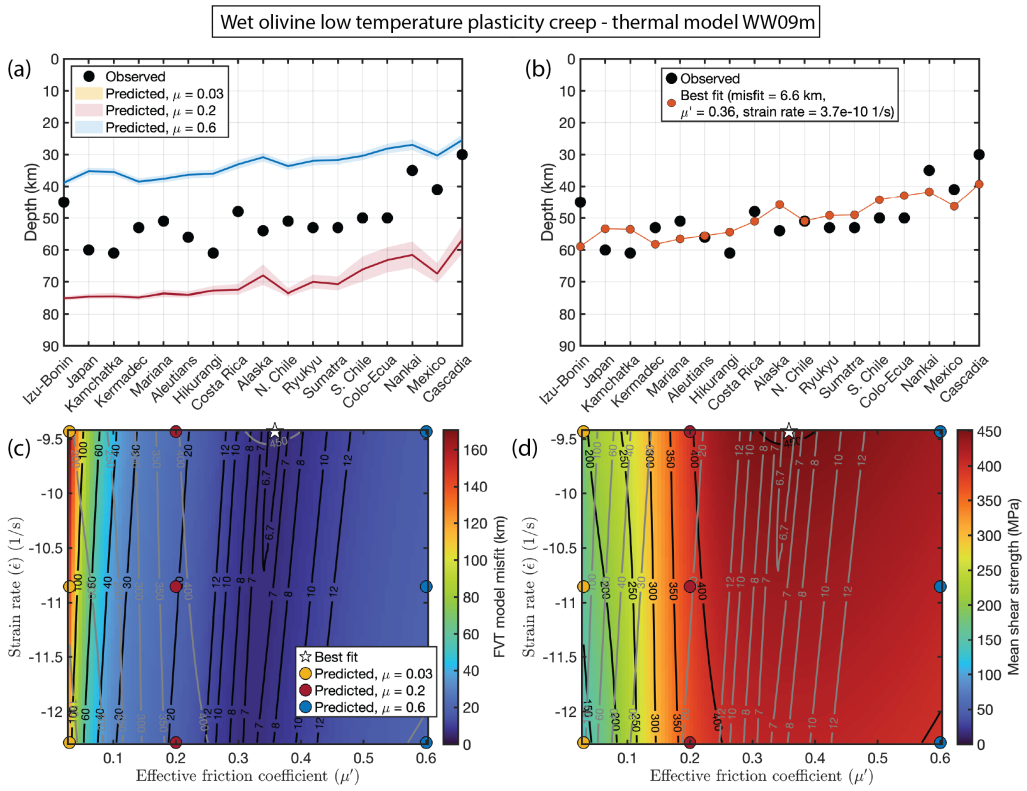

Figure 16: FVT inversion for wet olivine LTP with thermal model WW09m. (a) Lab constrained forward models. (b) Best fitting model between $\mu' = 0.03 - 0.6$ and $\dot{\epsilon} = 5.2 \times 10^{-13} - 3.7 \times 10^{-10}$ 1/s. (c) Grid search with black lines as root-mean-square misfit contours. Gray contours are mean shear strength. White star denotes best fitting model shown in (b) and circles are parameters of forward models plotted in (a). (d) Same as (c) except for mean shear strength of all 17 subduction zones at the predicted FVT.

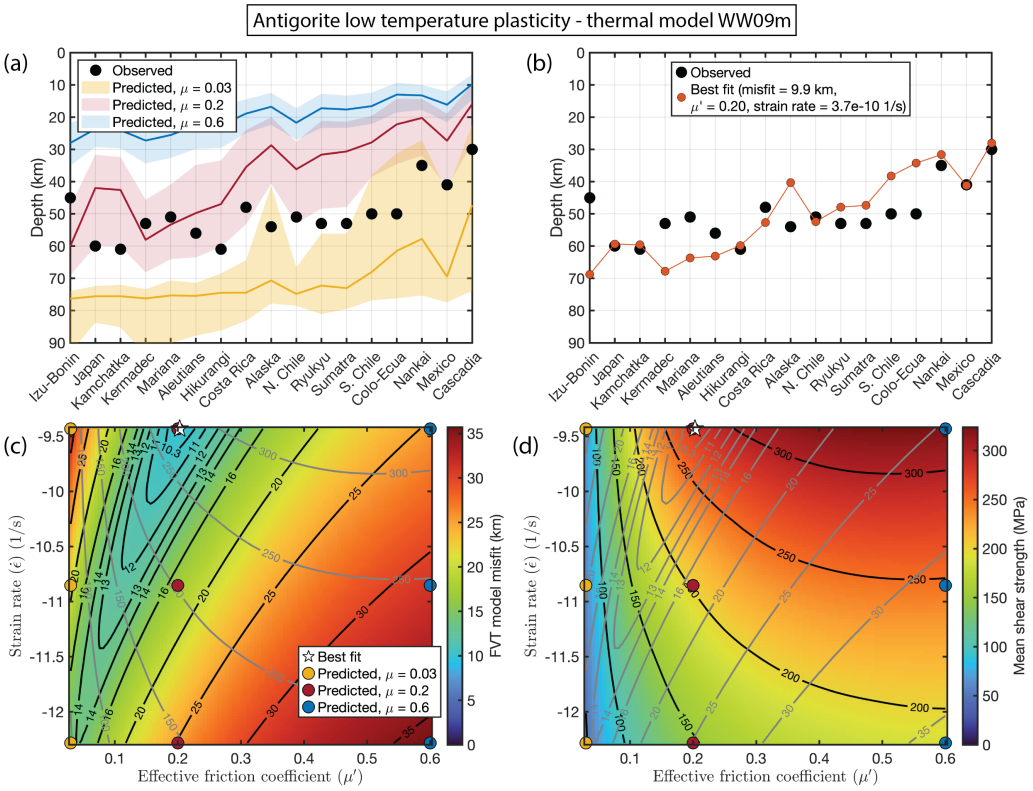

Figure 17: FVT inversion for antigorite LTP with thermal model WW09m. (a) Lab constrained forward models. (b) Best fitting model between $\mu' = 0.03 - 0.6$ and $\dot{\epsilon} = 5.2 \times 10^{-13} - 3.7 \times 10^{-10}$ 1/s. (c) Grid search with black lines as root-mean-square misfit contours. Gray contours are mean shear strength. White star denotes best fitting model shown in (b) and circles are parameters of forward models plotted in (a). (d) Same as (c) except for mean shear strength of all 17 subduction zones at the predicted FVT

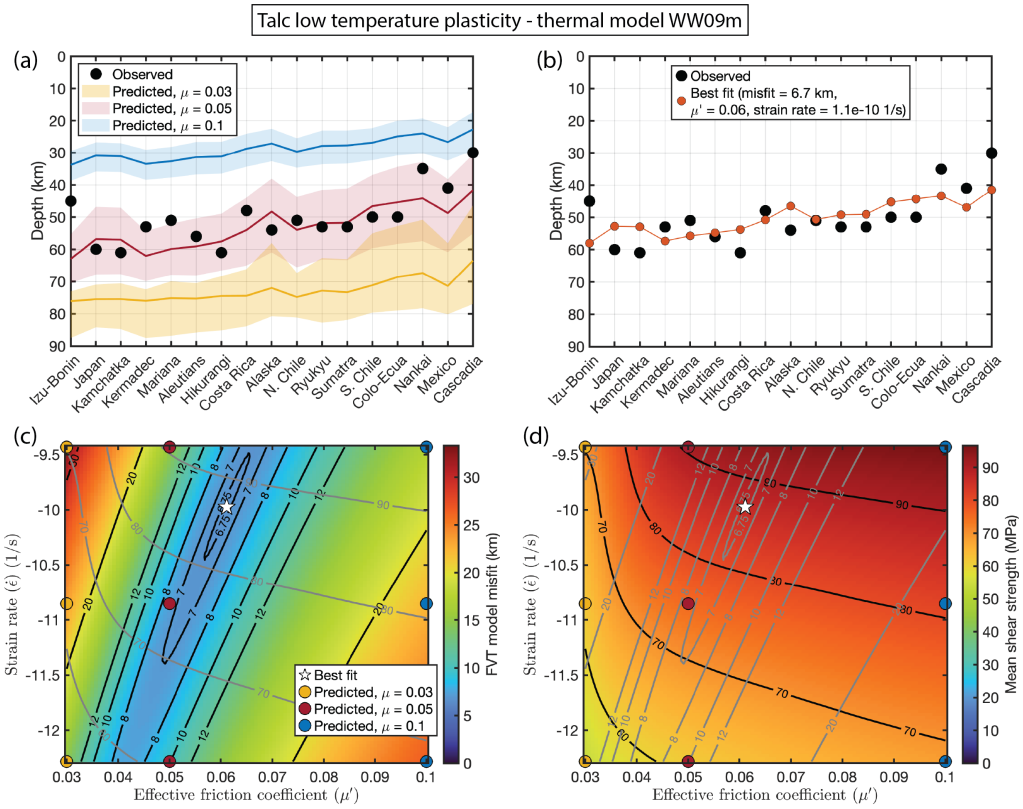

Figure 18: FVT inversion for talc LTP with thermal model WW09m. (a) Lab constrained forward models with $\mu' = 0.03$, 0.05, and 0.1 plotted due to talc weakness. (b) Best fitting model between $\mu' = 0.03 - 0.1$ and $\dot{\epsilon} = 5.2 \times 10^{-13} - 3.7 \times 10^{-10}$ 1/s. (c) Grid search with black lines as root-mean-square misfit contours. Gray contours are mean shear strength. White star denotes best fitting model shown in (b) and circles are parameters of forward models plotted in (a). (d) Same as (c) except for mean shear strength of all 17 subduction zones at the predicted FVT.

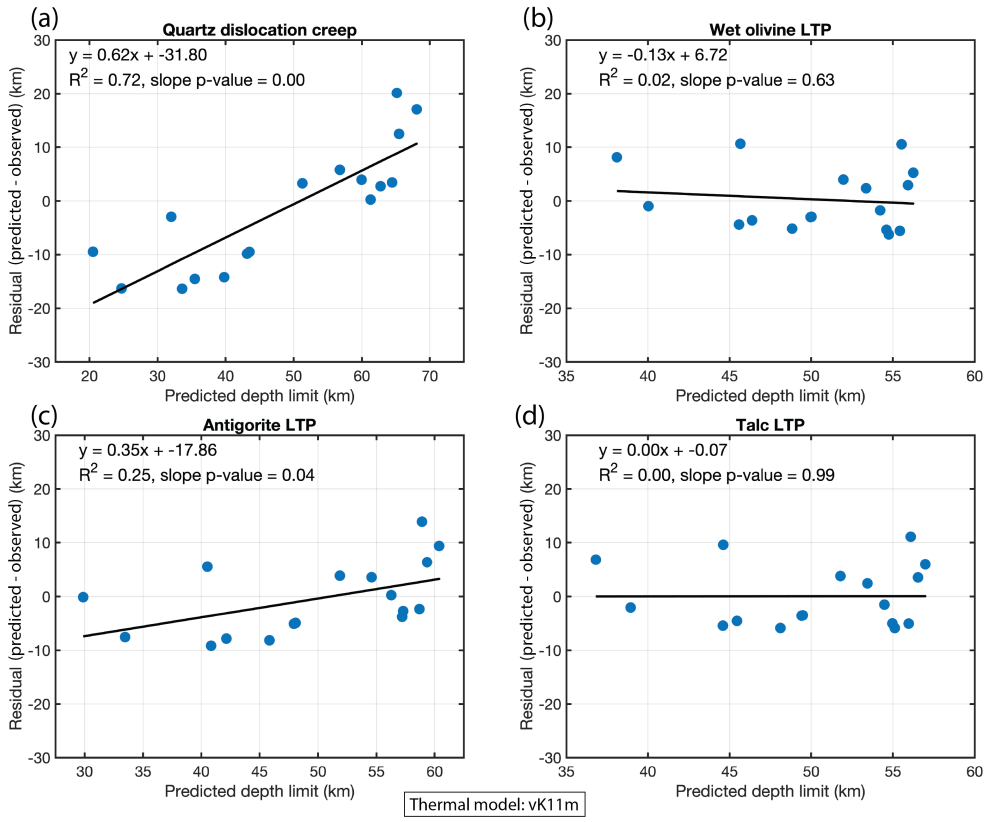

Figure 19: Residual analysis of predicted FVT from grid search inversions for thermal model vK11m. Residual values are predicted minus observed. Each blue circle is a single subduction zone. The predicted depth limits are all for the minimum misfit case shown for each creep mechanism. A line is fit to the residuals to quantify the correlation between predicted depth and model misfit.

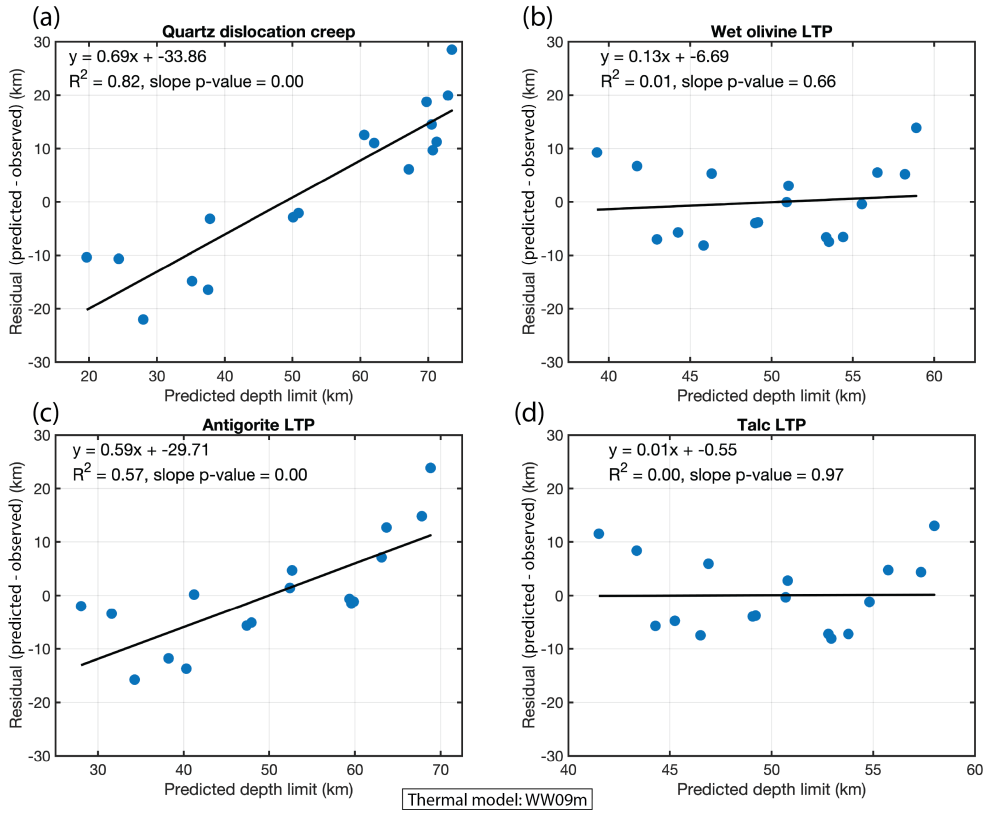

Figure 20: Same as Fig. 19 but for thermal model WW09m.

References

Bassett, D., Arnulf, A., Kodaira, S., Nakanishi, A., Harding, A., Moore, G., 2022. Crustal structure of the nankai subduction zone revealed by two decades of onshore-offshore and ocean-bottom seismic data: Implications for the dimensions and slip behavior of the seismogenic zone. Journal of Geophysical Research: Solid Earth 127, e2022JB024992. URL: https://doi.org/10.1029/2022JB024992.

Bassett, D., Henrys, S., Tozer, B., van Avendonk, H., Gase, A., Bangs, N., Kodaira, S., Okaya, D., Jacobs, K., Sutherland, R., et al., 2025. Crustal structure of the hikurangi subduction zone revealed by four decades of onshore-offshore seismic data: Implications for the dimensions and slip behavior of the seismogenic zone. Journal of Geophysical Research: Solid Earth 130, e2024JB030268. URL: https://doi.org/10.1029/2024JB030268.

Blanpied, M., Marone, C., Lockner, D., Byerlee, J., King, D., 1998. Quantitative measure of the variation in fault rheology due to fluid-rock interactions. Journal of Geophysical Research: Solid Earth 103, 9691–9712. URL: https://doi.org/10.1029/98JB00162.

Bletery, Q., Thomas, A.M., Rempel, A.W., Karlstrom, L., Sladen, A., De Barros, L., 2016. Mega-earthquakes rupture flat megathrusts. Science 354, 1027–1031. URL: https://doi.org/10.1126/science.aag0482.

Dziewonski, A.M., Chou, T.A., Woodhouse, J.H., 1981. Determination of earthquake source parameters from waveform data for studies of global and regional seismicity. Journal of Geophysical Research: Solid Earth 86, 2825–2852. URL: https://doi.org/10.1029/JB086iB04p02825.

Engdahl, E.R., van der Hilst, R., Buland, R., 1998. Global teleseismic earthquake relocation with improved travel times and procedures for depth determination. Bulletin of the Seismological Society of America 88, 722–743. URL: https://doi.org/10.1785/BSSA0880030722.

Fisher, D.M., Hirth, G., 2024. A pressure solution flow law for the seismogenic zone: Application to cascadia. Science Advances 10, eadi7279. URL: https://doi.org/10.1126/sciadv.adi7279.

Gao, X., Wang, K., 2014. Strength of stick-slip and creeping subduction megathrusts from heat flow observations. Science 345, 1038–1041. URL: https://doi.org/10.1126/science.1255487.

Gao, X., Wang, K., 2017. Rheological separation of the megathrust seismogenic zone and episodic tremor and slip. Nature 543, 416–419. URL: https://doi.org/10.1038/nature21389.

Hayes, G., 2023. Personal communication.

Hayes, G.P., Moore, G.L., Portner, D.E., Hearne, M., Flamme, H., Furtney, M., Smoczyk, G.M., 2018. Slab2, a comprehensive subduction zone geometry model. Science 362, 58–61. URL: https://doi.org/10.1126/science.aat4723.

He, C., Wang, Z., Yao, W., 2007. Frictional sliding of gabbro gouge under hydrothermal conditions. Tectonophysics 445, 353–362. URL: https://doi.org/10.1016/j.tecto.2007.09.008.

Heuret, A., Lallemand, S., Funiciello, F., Piromallo, C., Faccenna, C., 2011. Physical characteristics of subduction interface type seismogenic zones revisited. Geochemistry, Geophysics, Geosystems 12. URL: https://doi.org/10.1029/2010GC003230.

Igarashi, T., Matsuzawa, T., Hasegawa, A., 2003. Repeating earthquakes and interplate aseismic slip in the northeastern japan subduction zone. Journal of Geophysical Research: Solid Earth 108. URL: https://doi.org/10.1029/2002JB001920.

Igarashi, T., Matsuzawa, T., Umino, N., Hasegawa, A., 2001. Spatial distribution of focal mechanisms for interplate and intraplate earthquakes associated with the subducting pacific plate beneath the northeastern japan arc: A triple-planed deep seismic zone. Journal of Geophysical Research: Solid Earth 106, 2177–2191. URL: https://doi.org/10.1029/2000JB900386.

Katsura, T., 2022. A revised adiabatic temperature profile for the mantle. Journal of Geophysical Research: Solid Earth 127, e2021JB023562. URL: https://doi.org/10.1029/2021JB023562.

Kawakatsu, H., Seno, T., 1983. Triple seismic zone and the regional variation of seismicity along the northern honshu arc. Journal of Geophysical research: Solid Earth 88, 4215–4230. URL: https://doi.org/10.1029/JB088iB05p04215.

van Keken, P.E., Hacker, B.R., Syracuse, E.M., Abers, G.A., 2011. Subduction factory: 4. depth-dependent flux of h2o from subducting slabs worldwide. Journal of Geophysical Research: Solid Earth 116. URL: https://doi.org/10.1029/2010JB007922.

van Keken, P.E., Wada, I., Abers, G.A., Hacker, B.R., Wang, K., 2018. Mafic high-pressure rocks are preferentially exhumed from warm subduction settings. Geochemistry, Geophysics, Geosystems 19, 2934–2961. URL: https://doi.org/10.1029/2018GC007624.

Lange, D., Rietbrock, A., Haberland, C., Bataille, K., Dahm, T., Tilmann, F., Flüh, E., 2007. Seismicity and geometry of the south chilean subduction zone (41.5 s–43.5 s): Implications for controlling parameters. Geophysical Research Letters 34. URL: https://doi.org/10.1029/2006GL029190.

Morton, E.A., Bilek, S.L., Rowe, C.A., 2023. Cascadia subduction zone fault heterogeneities from newly detected small magnitude earthquakes. Journal of Geophysical Research: Solid Earth 128, e2023JB026607. URL: https://doi.org/10.1029/2023JB026607.

Oleskevich, D., Hyndman, R., Wang, K., 1999. The updip and downdip limits to great subduction earthquakes: Thermal and structural models of cascadia, south alaska, sw japan, and chile. Journal of Geophysical Research: Solid Earth 104, 14965–14991. URL: https://doi.org/10.1029/1999JB900060.

Seno, T., 2005. Variation of downdip limit of the seismogenic zone near the japanese islands: Implications for the serpentinization mechanism of the forearc mantle wedge. Earth and Planetary Science Letters 231, 249–262. URL: https://doi.org/10.1016/j.epsl.2004.12.027.

Sherrill, E.M., Johnson, K.M., Jackson, N., 2024. Locating boundaries between locked and creeping regions at nankai and cascadia subduction zones. Journal of Geophysical Research: Solid Earth 129, e2024JB029346. URL: https://doi.org/10.1029/2024JB029346.

USGS, 2018. Search earthquake catalog. URL: http://earthquake.usgs.gov/earthquakes/search/.

Wada, I., Wang, K., 2009. Common depth of slab-mantle decoupling: Reconciling diversity and uniformity of subduction zones. Geochemistry, Geophysics, Geosystems 10. URL: https://doi.org/10.1029/2009GC002570.

Wallace, L.M., Beavan, J., Bannister, S., Williams, C., 2012. Simultaneous long-term and short-term slow slip events at the hikurangi subduction margin, new zealand: Implications for processes that control slow slip event occurrence, duration, and migration. Journal of Geophysical Research: Solid Earth 117. URL: https://doi.org/10.1029/2012JB009489.

Wallace, L.M., Reyners, M., Cochran, U., Bannister, S., Barnes, P.M., Berryman, K., Downes, G., Eberhart-Phillips, D., Fagereng, A., Ellis, S., et al., 2009. Characterizing the seismogenic zone of a major plate boundary subduction thrust: Hikurangi margin, new zealand. Geochemistry, Geophysics, Geosystems 10. URL: https://doi.org/10.1029/2009GC002610.

Wang, K., Tréhu, A.M., 2016. Invited review paper: Some outstanding issues in the study of great megathrust earthquakes—the cascadia example. Journal of Geodynamics 98, 1–18. URL: https://doi.org/10.1016/j.jog.2016.03.010.